Performance Comparison of Ni/TiO_2 and Au/TiO_2 Photocatalysts for H_2 Production in Different Alcohol-Water Mixtures

Wan-Ting Chen[a], Andrew Chan[a], Jordi Llorca[b], Dongxiao Sun-Waterhouse[a], Hicham Idriss[c], Geoffrey I.N. Waterhouse*[a,d]

[a]School of Chemical Sciences, The University of Auckland, Auckland, New Zealand.
[b]Institute of Energy Technologies and Centre for Research in NanoEngineering, Polytechnic University of Catalonia, Digonal 647, 08028 Barcelona, Spain.
[c]SABIC, Corporate Research Institute (CRI), KAUST, Saudi Arabia.
[d]The MacDiarmid Institute for Advanced Materials and Nanotechnology, New Zealand.

*Corresponding author:
Email: g.waterhouse@auckland.ac.nz
Telephone number: 64-9-9237212
Fax number: 64-9-373 7422

Highlights:

- Ni/TiO_2 and Au/TiO_2 photocatalysts afford similar H_2 rates in alcohol-water mixtures under UV.
- Ni/TiO_2 outperforms Au/TiO_2 in methanol-water mixtures.
- H_2 production rates depend on the alcohol hole scavenger ad alcohol concentration.
- At 10 vol.%, rates follow the order glycerol > ethylene glycol > methanol > ethanol.
- At 70 vol.%, rates follow the order methanol > ethanol > ethylene glycol > glycerol.

Abstract

This study systematically compares the performance of Ni/P25 TiO_2 and Au/P25 TiO_2 photocatalysts for H_2 production in alcohol-water mixtures under UV excitation. 0.5 wt. % Ni/P25 TiO_2 and 2 wt.% Au/P25 TiO_2 photocatalyst were synthesized using literature procedures. HRTEM, UV-Vis, XANES and EXAFS analyses confirmed the presence of 5-8 nm metallic Ni and Au nanoparticles on the surface of the respective photocatalysts. H_2 production tests were conducted in various alcohol-water systems (0-100 vol.%), using methanol, ethanol, ethylene glycol and glycerol. The Ni/P25 TiO_2 and Au/P25 TiO_2 photocatalysts demonstrated remarkably similar performance for hydrogen production in all

the alcohol-water systems tested, with Ni/P25 TiO_2 being marginally superior in methanol-water mixtures. At low alcohol concentrations (15 vol.% or less), rates followed the order glycerol > ethylene glycol > methanol > ethanol, whilst at higher alcohol concentrations methanol (optimum 40 vol.%) and ethanol (optimum 80-90 vol.%) afforded the highest H_2 production rates.

Keywords Hydrogen production; alcohol photoreforming; photocatalysis; nickel; TiO_2

1. Introduction

Hydrogen (H_2) is widely considered to be the clean energy vector of the future, with the gradual transition from a fossil fuel economy to a hydrogen economy expected to take place over the next 50-100 years. This transition demands low cost and environmentally friendly methods for H_2 production, distribution and storage, with the former arguably the greatest obstacle to the development of a sustainable hydrogen economy [1-3]. Currently, H_2 is produced industrially via steam methane reforming (SMR) coupled the water/gas shift reaction [2, 4, 5], processes which are energy intensive and have a significant carbon footprint. Amongst the various alternative technologies that have been proposed for future hydrogen production, water-splitting and alcohol-photoreforming using sunlight and semiconductor photocatalysts represent two of the more promising pathways. Over the past decade, an enormous amount of research effort has been directed towards the development and optimization of semiconductor photocatalysts for solar hydrogen production, with M/TiO_2 photocatalysts (M = Pd, Pt or Au) dominating this research space due to their high activity and photo-corrosion resistance [6-14].

A wide range of semiconductor materials have been studied in relation to H_2 production from water or biofuels under UV or solar excitation. TiO_2 (E_g = 3.0-3.3 eV, depending on the polymorph) is the most studied of these semiconductor because it low cost and satisfies the following three essential requirements to be an effective H_2 production photocatalyst [15, 16]: 1) the valence band of TiO_2 is more positive than the O_2/H_2O redox couple (+1.23 V versus NHE) or that of typical hole scavengers such as ethanol (CH_3CHO/CH_3CH_2OH +0.19 V versus NHE); (2) the conduction band of TiO_2 is more negative than the H_2O/H_2 redox couple (0 V versus NHE); and (3) TiO_2 is resistant to photocorrosion under UV excitation and the photoreactions that generate H_2 [6, 7]. Bulk absorption of electromagnetic radiation with E > E_g generates electron-hole pairs (e^- - h^+), which either recombine or migrate to the surface of

TiO_2 particles and drive oxidation and reducing reactions, respectively. However, bare TiO_2 surfaces are ineffective for generating H_2, due to the rapid electron-hole pair recombination and the large overpotential on TiO_2 surfaces. Surface modification of TiO_2 with electron accepting co-catalysts (e.g. especially Pd, Pt, Pt and Au) [12-14, 17-22] or semiconductors (e.g. Cu_2O, CuO) [3, 23-25] is effective in promoting H_2 evolution by suppressing electron-hole pair recombination (increasing the availability of charge carriers) and also creating cathodic sites for H_2 evolution. The best metal co-catalysts are high work function metals ((Pd ϕ = 5.6 eV, Pt ϕ = 5.7 eV and Au ϕ = 5.3-5.6 eV) which form effective Schottky junctions with TiO_2 [26, 27], thereby allowing them to accept electrons from the conduction band of TiO_2. The Fermi level of these metal co-catalysts located between bottom of TiO_2 conduction band and the H_2O/H_2 redox couple, allowing facile transfer of electrons from TiO_2 to the metal co-catalysts and subsequently to aqueous protons in solution. Amongst the alternatives to active through expensive platinum group metal co-catalysts (Pd, Pt and Au), metallic nickel (Ni) is the most logical candidate, since Ni is cheap, abundant and similarly has a high work function (Ni ϕ = 5.3 eV) [26-28]. Relative to M/TiO_2 systems (Pd, Pt and Au), surprising little work has been reported to date on Ni/TiO_2 photocatalysts for H_2 production, motivating further investigation.

Work to date on Ni/TiO_2 systems has been hampered by uncertainty about the exact nature of the dispersed Ni-related species on TiO_2 responsible for promoting H_2 evolution (e.g. NiO [29-35], Ni [28, 36-39] or Ni-NiO [13, 40, 41]. Table 1 summarises literature on Ni/TiO_2 semiconductor photocatalysts for H_2 production. Fan et al. reported that NiO/TiO_2 interfaces form effective p-n heterojunctions which facilitate H_2 evolution under UV excitation by acting as electron-trapping sites [29]. TiO_2 is an intrinsic n-type semiconductor due to lattice oxygen vacancies, whereas NiO is a wide band gap p-type semiconductor (E_g = 3.6-4.0 eV) [42, 43] After photoexcitation of TiO_2, it was proposed that the electrons will migrate to NiO, which acts as the proton reduction site. Other groups have suggested that Ni/NiO core/shell structures can activate TiO_2 for H_2 evolution [13, 40, 41]. Bahruji et al. found $Ni\text{-}NiO/TiO_2$ photocatalysts yielded better photocatalytic activity compared to NiO/TiO_2 photocatalysts under the same testing conditions [13]. Recently, Chen et al. conducted a detailed study of Ni/TiO_2 photocatalysts for H_2 production in ethanol-water mixtures under UV excitation [28]. It was determined by XPS and Ni K-edge and Ni L-edge XANES that Ni^0 was the dominant nickel species on the surface of the Ni/TiO_2 photocatalysts, with the optimal Ni loading for hydrogen production being 0.5 wt.%. Indeed, the 0.5 wt.% Ni/TiO_2 photocatalyst prepared using Degussa P25 (85 wt.% anatase + 15 wt.% rutile) demonstrated superior photocatalytic activity to a 2

wt.% Au/P25 TiO_2 reference photocatalyst (2 wt.% loading is optimal for Au co-catalysts on TiO_2) at low ethanol concentrations (<10 vol.%). Chen et al. also tested NiO/TiO_2 photocatalysts in ethanol-water mixtures under UV [28], but these showed negligible initial activity and a long induction period before H_2 evolution commenced, suggesting reduction of NiO to Ni^0 via electron transfer from the TiO_2 conduction band occurred during UV irradiation to create active sites for H_2 evolution. It should be noted that H_2 production rates reported by Chen et al. were 1-2 orders of magnitude higher than in other literature studies (~10-20 mmol g^{-1} h^{-1} depending on the ethanol concentration, see Table 1), which suggests the need for caution and the requirement for further studies to confirm the high rates achieved. Further studies are also needed to confirm Ni^0 as the active co-catalyst species.

The addition of sacrificial hole scavengers such as methanol or ethanol is a commonly used practice in semiconductor photocatalysis to facilitate electron-hole pair separation following photoexcitation. The sacrificial hole scavengers act as electron donors and are progressively oxidised by valence band holes at the photocatalyst surface (e.g. $CH_3OH + 2h^+ \rightarrow HCHO + 2H^+$; $HCHO + H_2O + 2h^+ \rightarrow HCOOH + 2H^+$; $HCOOH + 2h^+ \rightarrow CO_2 + 2H+$), serving also as additional proton sources for generating H_2 [21, 22, 44-47]. The oxidation potentials for alcohol photoreforming alcohols are much lower than that of water (c.f. $CH_3OH + H_2O + 6h^+ \rightarrow CO_2 + 6H^+$, 0.03 V versus NHE; $CH_3CH_2OH + 3H_2O + 12h^+ \rightarrow 2CO_2 + 12H^+$, 0.08 V versus NHE; $H_2O \rightarrow H_2 + 1/2O_2$, 1.23 V versus NHE) [48]. Due to the relative ease of alcohol oxidation, and the suppression of electron-hole pair recombination in the semiconductor in the presence of the alcohol, photocatalytic H_2 production rates in alcohol-water mixtures are typically 1-2 orders of magnitude higher than those achieved in pure water. It should be noted that due to the higher charge carrier concentrations, the water splitting reaction is also enhanced when alcohols are used as sacrificial reagents. H_2 production rates are strongly dependent on the hole scavenger used [11-14, 21, 28, 49-53]. Bowker et al. investigated the Au/P25 TiO_2 system under UV, and found that H_2 production rates decreased in the order methanol > 1-propanol > ethanol > 1-butanol > 2-propanol >> tertiary butanol at a fixed alcohol concentration of 0.1 vol.% [11]. Bahruji et al. conducted a detailed study of the Pd/P25 TiO_2 system under UV using 20 different sacrificial reagents, and established the reactivity order triols > diols > 2^o alcohols > 1^o alcohols > 3^o alcohols again at a 0.1 vol.% alcohol concentration [49]. Yang et al. studied H_2 production from pure alcohols over a 1 wt.% Pt/anatase photocatalyst, and observed that rates decreased in the order methanol ≈ ethanol > 1-propanol ≈ 2-propanol > 1-butanol [14]. Recent studies have attempted to correlate hydrogen production rates with specific properties of the alcohol, such as structure, polarity, polarizability and alcohol oxidation potential [14].

These studies provide a reasonable guide as to the general reactivity pattern followed by M/TiO_2 photocatalysts at a specific alcohol concentrations.

What is not clear in current literature is the influence of alcohol concentrations on photocatalytic hydrogen production rates in M/TiO_2 systems (the vast majority of studies reported to date have used a single alcohol concentration, typically 0.1-0 vol.%). Only a few studies have probed the effect of alcohol concentration in detail [28, 54-61]. Wu et al. reported efficient hydrogen production from aqueous methanol-water mixtures containing Au/TiO_2 photocatalysts under UV irradiation [54]. The optimal methanol concentration was 5 M methanol, yielding a H_2 production rate of ~1000 μmol h^{-1}. Stelmachowski et al. examined a wide range of TiO_2-based photocatalysts (co-catalysts = W, Mn, Cr, Ni, Co, Pt, Pd, Au and Ag) in aqueous glycerol solutions [55]. The highest H_2 production rate achieved was 24.2 mmol g^{-1} h^{-1} for a 0.042 wt.% Pt/TiO_2 at a glycerol concentration of 4.5 wt.%. Daskalaki et al. conducted a systemic study of Pt/TiO_2 in glycerol-water mixtures [57]. The optimium reaction conditions were 0.1-0.5 wt.% Pt and a glycerol concentration of 1 M. Sadanandam et al. studies H_2 production from a 1 wt.% Co/TiO_2 photocatalyst in a range of glycerol-water mixtures (1-20 vol.%) under UV excitation, reporting an optimum H_2 production rate of 11021 μmol g^{-1} h^{-1} in 5 vol.% glycerol-water mixtures [61]. Recently, Chen et al. compared the photocatalytic activity of 0.5 wt.% Ni/TiO_2 and 2 wt.% Au/TiO_2 photocatalysts in a wide range of ethanol-water mixtures (0-100 vol.% alcohol) under UV irradiation [28]. The optimal ethanol concentration was 95 vol.% for Ni/TiO_2 (rate = 24.3 mmol g^{-1} h^{-1}) and 80 vol.% for Au/TiO_2 (rate = 32.4 mmol g^{-1} h^{-1}). To our knowledge, no study has yet been reported comparing the performance of different M/TiO_2 photocatalysts in different alcohol-water systems (e.g. methanol-water, ethanol-water, ethylene glycol-water and glycerol-water) and at different alcohol concentrations (e.g. 0-100 vol.%). It is not clear at all presently whether different M/TiO_2 photocatalysts (e.g. M = Ni, Pd, Pt, Au) show the same general H_2 production patterns with alcohol type and alcohol concentration, motivating a detailed experimental investigation.

This study aimed to systematically compares the performance of a 0.5 wt.% Ni/P25 TiO_2 photocatalyst and a 2 wt.% Au/P25 TiO_2 photocatalyst for H_2 production in different alcohol-water systems under UV excitation, placing particular emphasis on the effect of alcohol type (methanol, ethanol, ethylene glycol and glycerol) and alcohol concentration (0-100 vol.%) on H_2 production rates. The objectives of the study were 4-fold; (i) to compare the activity of Ni/TiO_2 and Au/TiO_2 photocatalysts for H_2 production in a wide range of alcohol-water mixtures under exactly the same testing conditions; (ii) to rank the alcohol sacrificial agents in terms of their ability to promote hydrogen evolution as a function of alcohol concentration; (iii)

for each alcohol, to determine the optimum alcohol concentration for H_2 production; (iv) to further explore relationships between photocatalytic H_2 production rates and specific properties of the alcohols (such as the standard oxidation potential or viscosity of the alcohol-water mixtures). The overarching aim of the study was to validate the potential of Ni/TiO_2 photocatalysts as low cost alternatives to Au/TiO_2 photocatalysts for solar H_2 production in alcohol-water mixtures.

2. Experimental Section

2.1. Materials

Nickel(II) nitrate hexahydrate (≥97 %), glycerol (≥99 %), urea (≥99.5 %), sodium hydroxide (≥98 %), ammonia (28 wt.%), H_2O_2 (30 vol.%), HF (40 wt.%), Degussa P25 TiO_2, absolute ethanol (≥99.5 %), Ni foil (99.99%) and NiO (≥99.9 %) were all obtained from Sigma-Aldrich and used without further purification. All solutions were prepared using milli-Q water (18.2 MΩ·cm resistivity). A reference photocatalyst, 2 wt.% Au/P25 TiO_2, was prepared using the deposition-precipitation with urea method described by Zanella et al. [62]. Relevant characterization data for the 2 wt.% Au/TiO_2 reference photocatalyst is provided in reference [63].

2.2. NiO/P25 TiO_2 and Ni/P25 TiO_2 photocatalyst synthesis

A NiO/P25 TiO_2 (NiO loading = 0.63 wt.%) photocatalyst precursor was prepared by the complex precipitation method [64]. Briefly, nickel(II) nitrate hexahydrate and glycerol (1:2 molar ratio) were added to milli-Q water (200 mL) to form an aqueous nickel(II)-glycerol complex. The exact mass of nickel (II) nitrate hexahydrate and glycerol were 0.247 g and 0.16 g, repsectively. P25 TiO_2 (10 g) was then added to the solution containing the nickel(II)-glycerol complex with continuous stirring. The nickel-glycerol complex was then precipitated on the P25 TiO_2 support by the dropwise addition of 0.5 M NaOH under constant stirring until a pH of 12 was reached. The resulting suspension was stirred for a further 1 h, and then the resulting light green powder (i.e. $Ni(OH)_2$/P25 TiO_2) collected by vacuum filtration. After washing repeatedly with milli-Q water, the $Ni(OH)_2$/P25 TiO_2 powder was dried overnight at 70 °C in air. The 0.63 wt.% NiO/P25 TiO_2 photocatalyst were obtained by calcination of the $Ni(OH)_2$/P25 TiO_2 powder at 300 °C for 2 h.

The 0.5 wt.% Ni/P25 TiO_2 photocatalyst was obtained by heating the 0.63 wt.% NiO/P25

TiO_2 precursor under a H_2/N_2 flow (10 vol.% H_2, 100 mL min^{-1}) at 500 °C for 2 h. This treatment reduced adsorbed Ni(II) species to metallic form as evidence by a change in the colour of the powders from green (characteristic of NiO) to grey (characteristic of finely dispersed Ni^0) [65]. Detailed physico-chemical characterization studies were subsequently conducted on both the NiO/P25 TiO_2 precursor and Ni/P25 TiO_2 photocatalyst.

2.3. Isolation of anatase and rutile from P25 TiO_2

To examine the role of anatase-rutile heterojunctions in P25 TiO_2 in promoting H_2 production, anatase and rutile nanoparticles were isolated from P25 TiO_2 by selective chemical dissolution using procedures described by Ohtani et al. and Ohno et al., respectively [66, 67]. The anatase component was isolated as follows. Aqueous ammonia (2.5 wt.%, 20 mL) was added dropwise to a chilled aqueous H_2O_2 solution (30 wt.%, 600 mL) with constant stirring. Degussa P25 TiO_2 powder (5.40 g) was then added to the NH_3-H_2O_2 solution Degussa P25 TiO_2 powder (5.40 g) was then added to the NH_3-H_2O_2 solution stirring and the resulting suspension stirring for 12 h at room temperature. The anatase product was then collected by centrifugation at 4400 rpm for 30 min and the yellow supernatant discarded. The anatase powder was washed repeatedly with water and then oven dried at 100 °C for 24 h. The rutile component was isolated by adding P25 TiO_2 (30 g) to a 7 wt.% of aqueous HF solution (1 L) with constant stirring for 24 h at 20 °C. The residual powder was collected by centrifugation at 4400 rpm for 30 min, and the supernatant discarded. The rutile powder was washed repeatedly with Milli-Q and then calcined at 550 °C in air for 2 h to remove any residual fluroide. In the text below, the isolated anatase and rutile powders are referred to as anatase and rutile, respectively. A 0.5 wt.% Ni/anatase and 0.5 wt.% Ni/(85% anatase + 15% rutile) photocatalysts were then prepared using the method described in section 2.2. For the preparation of the latter, a physical mixture of isolated anatase (85 wt.%) and isolated rutile (15 wt.%) was first prepared. This had the same weight fractions of anatase and rutile as P25 TiO_2, but no anatase-rutile heterojunctions. Relevant characterization data for the isolate anatase and rutile phases is provided in reference [68].

2.4. Photocatalyst characterization

UV-Visible absorbance spectra were recorded over the range 250-1400 nm on a Shimadzu UV-2101 PC spectrophotometer equipped with an **ISR-240A integrating sphere attachment.** Barium sulphate was used as a reflectance standard.

TEM images were collected using a TECNAI 12 transmission electron microscope, operated at an electron accelerating voltage of 120 kV. Powder samples were dispersed in absolute ethanol and then 1 μL of the resulting dispersion placed on carbon coated copper TEM grids for analysis.

HRTEM microstructural characterization was performed using a JEOL 2010F transmission electron microscope equipped with a field emission source operated at 200 kV. The point-to-point resolution of the electron microscope was 0.19 nm, and the resolution between lines was 0.14 nm. For STEM-HAADF-EDX characterization, the instrument used was a Tecnai G^2 F20 S-TWIN microscope equipped with a field emission electron source operated at 200 kV. The point-to-point resolution was 0.24 nm and the resolution between lines was 0.10 nm. Samples were deposited from alcohol suspensions onto holey-carbon Cu grids for analysis.

Powder XRD patterns were taken on a PANalytical Empyrean diffractometer equipped with a Cu anode X-ray tube and a curved graphite filter monochromator. XRD data was collected from 2θ = 10-90˚ (step 0.02º, scan rate 2º min^{-1}) using Cu Kα X-rays (λ = 1.5418 Å, 40 mA, 40 kV). Anatase and rutile crystallite sizes (L) were determined from the powder XRD data using the Scherrer equation and line-widths of the anatase (101) reflection at 2θ = 25.3º and rutile (110) reflection at 2θ = 27.4º, respectively. The rutile:anatase ratio in the samples was determined according to the method described by Ding et al. [69].

$$\%Rutile = \frac{1}{\left[1 + 0.8(I_A / I_R)\right]} \times 100$$

Where I_A is the peak intensity for the anatase (101) reflection, and I_R is the peak intensity for the rutile (110) reflection.

Ni K-edge EXAFS data was collected on the BL01B1 beamline of the Japan Synchrotron Radiation Research Institute (SPring-8). The storage ring was operated at 8 GeV and a ring current of 44-65 mA. A Si(111) single crystal was used to monochromatize the X-ray beam, and two ion chambers filled with Ar and N_2 were used as detectors of I_0 and I, respectively. 1 wt.% Ni/TiO_2 and 1.25 wt.% NiO/TiO_2 photocatalysts were pressed into thin pellets for the

EXAFS measurements, with a specific pellet thickness and density chosen to achieve an edge jump of ~0.4. All data reported here was collected in transmission mode. For EXAFS analysis, the oscillations were extracted from the EXAFS data by a spline smoothing method, and then normalized by the edge height around 50 eV above the absorption threshold. R-space plots were obtained by performing a Fourier transformation of the k^3-weighted EXAFS oscillation from *k*-space to *r*-space over the range 30-140 nm^{-1}. *In-situ* quick XAFS (QXAFS) analyses were performed following a similar procedure to Okumura et al. [70]. Briefly, 0.63 wt.% NiO/P25 TiO_2 samples were pressed into 1 mm thick pellets of 7 mm diameter. Multiple pellets were stacked in a custom built quartz holder to achieve an edge jump of 0.3 or greater. The holder was then transferred into an aluminium cell sealed by Kapton windows and connected to a gas flow reaction system. Flow cell gas concentrations were carefully monitored using a quadrapole mass spectrometer in real time. *In-situ* XAFS analyses on Ni K-edge were carried out at 60 s intervals at 400 °C in O_2:He gas or H_2:He gas at a fixed volume ratio of 1:99 for Ni species oxidation and reduction cycles..

N_2 physisorption isotherms were determined at liquid nitrogen temperature (-195 °C) using a Micromeritics Tristar 3000 instrument. Specific surface areas were calculated from the N_2 adsorption data according to the Brunauer-Emmett-Teller (BET) method using P/P_0 values in the range 0.05-0.2 [71]. Cumulative pore volumes and pore diameters were calculated from the adsorption isotherms by the Barrett-Joyner-Halenda (BJH) method [72]. Samples were degassed at 100 °C under vacuum for 1 h prior to the N_2 physisorption measurements. All samples had similar N_2 physisorption isotherms that could be classified as Type II according to the IUPAC convention for adsorption isotherms.

Photoluminescence measurements were performed in air at room temperature using a Perkin-Elmer LS-55 Luminescence Spectrometer. A 290 nm cutoff filter was used. Spectra were excited at 310 nm and photoluminescence spectra were recorded over a range of 330-600 nm using a standard photomultiplier.

2.5. Photocatalytic hydrogen production tests

Photocatalytic hydrogen production tests on the Ni/P25 TiO_2, Ni/anatase, Ni/(85% anatase + 15% rutile) and Au/TiO_2 photocatalysts were carried out in a tubular pyrex reactor (105 mL volume). Photocatalyst (6.5 mg) was placed in the reactor and flushed under a N_2 flow for 30

min to remove oxygen. Then, 20 mL of an alcohol-water mixture (0-100 vol.% alcohol) was injected into the reactor through a rubber septum and the resulting photocatalyst dispersion stirred continuously for 1 h in the dark (no UV excitation). The reactor was then exposed to UV light, supplied from a Spectraline model SB-100P/F lamp (100 W, 365 nm) at a distance of 10 cm from the reactor. The photon flux at the sample was approximately 6.5 mW cm^{-2} (the UV flux from the Sun is approximately 5 mW cm^{-2}). Hydrogen evolution was monitored by taking gas head space samples (1 mL) at 20 min intervals and injecting these into a Shimadzu GC 2014 equipped with a TCD detector and Carboxen-1010 plot capillary column (L×I.D. 30 m×0.53 mm, average thickness 30 μm). H_2 evolved was quantified against an external calibration curve of peak area versus moles of H_2. Photocatalytic tests for each sample were carried out in triplicate.

3. Results and Discussion

3.1. Photocatalyst characterization

Transmission electron microscopy (TEM) analyses were conducted on the various Ni/TiO_2 and Au/TiO_2 photocatalysts to establish the approximate mean size and dispersion of the supported Ni and Au co-catalysts. Metallic Ni nanoparticles were difficult to discern by conventional TEM for the 0.5 wt.% Ni/TiO_2 photocatalysts due to the similarity in the atomic number of Ni and Ti. However, using HRTEM and EDX, Ni nanoparticles could be readily identified on the surface of the P25 TiO_2 support (Fig. 1(a)-(e)). EDX spectra recorded over the low and high contrast areas “a” and “b” in STEM/HADADF imaging mode allowed classification of Ni and TiO_2 particles (Fig. 1(a)-(b)). The low contrast areas are TiO_2 and the high contrast areas are Ni-containing particles. To get a better insight into the nature and structure of the nickel-containing particles, HRTEM analysis was carried out and the location of Ni nanoparticles indicated in Fig. 1(c). At the nominal Ni loading of 0.5 wt.% (confirmed by XRF, Table 5), the Ni nanoparticles were ~5-8 nm in size. The metallic nature of the nanoparticles was confirmed by the detailed lattice fringe analysis provided in Fig. 1(d)-(e). Fig. 1(d) shows two anatase particles and a Ni nanoparticle oriented along the [110] crystallographic direction. The Fourier Transform image recorded over the Ni particle shows spots at 2.04 Å, corresponding to (111) crystallographic planes of Ni metal [70-72]. Fig. 1(e) shows an FT image with spots at 2.04 and 1.76 Å, correspond to the (111) and (200) crystallographic planes of Ni metal [70]. The HRTEM analyses confirm the presence of 5-8 nm Ni metal nanoparticles on the surface of the 0.5 wt.% Ni/P25 TiO_2 photocatalyst. It should

be noted that the HRTEM analysis was performed approximately 1 month after the H_2 reduction step used in the synthesis of the photocatalyst (to reduce supported NiO to Ni, section 2.2). This suggests that the re-oxidation of Ni to NiO proceeds very slowly at room temperature (this has important implications for H_2 production tests discussed below where we strongly advocate metallic Ni as the active co-catalyst for H_2 production). For the 2 wt.% Au/P25 TiO_2 photocatalyst, the mean size of the Au nanoparticles was also in the same range (5-8 nm), with the gold nanoparticles being easy to discern form the P25 support even at low magnification (Fig. 1(f)).

Powder XRD patterns for P25 TiO_2, 0.63 wt.% NiO/P25 TiO_2, 0.63 wt.% NiO/P25 TiO_2 and 2 wt.% Au/P25 TiO_2 are shown in Fig. S1. The XRD patterns for all photocatalysts were dominated by peaks due to anatase and rutile in the P25 TiO_2 support. The anatase:rutile weight ratio for all photocatalysts was ~6:1, in good agreement with the manufacturer's specifications. Average anatase and rutile particle sizes, estimated from the FWHM of the anatase (101) and rutile (110) reflections using the Scherrer equation, were 25 nm and 50 nm, respectively. The data confirms that co-catalyst deposition did not change the phase composition of the P25 TiO_2 support. No obvious diffraction patterns were seen for NiO or Ni were evident at low nominal metal loadings used here. For the 2 wt.% Au/P25 TiO_2 sample, very weak and broad peaks around 44º and 64º could be discerned and assigned to *fcc* Au(200) and Au(220) reflections, respectively (the Au(111) reflection is obscured by signals from the P25 TiO_2 support).

UV-Vis absorbance spectra and corresponding Tauc plots for P25 TiO_2, 0.63 wt.% NiO/P25 TiO_2, 0.5 wt.% Ni/TiO_2 and 2 wt.% Au/TiO_2 are shown in Fig. 2. All samples showed intense absorption below 400 nm due to the P25 TiO_2 support (E_g ~ 3.15 eV was determined from the Tauc plots for each photocatalyst). The 0.63 wt.% NiO/P25 TiO_2 photocatalyst precursor was a light green colour and showed distinctive absorption features at visible wavelengths corresponding to d-d transitions (electron configuration of Ni^{2+} is $3d^8$). In contrast, the 0.5 wt.% Ni/p25 TiO_2 photocatalyst prepared by H_2 reduction of the precursor was grey absorbing strongly across the entire visible spectrum consistent with the presence of supported metallic nickel nanoparticles. The Au/P25 TiO_2 photocatalyst showed an intense absorption feature centred between 560-590 nm, associated with the characteristic Au 5d → 6 sp localised surface plasmon resonance (LSPR) absorption of Au nanoparticles dispersed on TiO_2.

X-ray photoelectron spectroscopy (XPS) data for the 0.5 wt.% Ni/P25 TiO_2 and 2 wt.% Au/TiO_2 photocatalysts have been reported elsewhere [28], and confirmed that metallic Ni and Au were the dominant co-catalyst species on the surface of these photocatalysts. *In-situ* Ni K-edge X-ray absorption analyses were subsequently conducted to better understand the NiO to

Ni reduction process used to "activate" the Ni/TiO_2 photocatalysts for H_2 production. Au 4f XPS spectra shows the presence of metallic Au species in the 2 wt.% Au/TiO_2 photocatalysts.

These measurements were very useful for identifying the chemical state of nickel (metallic Ni or NiO) on P25 TiO_2 during reduction or oxidation treatments. For the experiments, pellets of the 0.63 wt.% NiO/P25 TiO_2 photocatalyst precursor were prepared, then transferred to an in-situ cell and subjected to alternating cycles of reduction (1 vol.% H_2 in He) and oxidation (1 vol.% O_2 in He) at 400 °C. A reduction temperature of 400 °C was selected so that the reduction process did not happen too quickly (note that we used a reduction temperature of 500 °C when preparing the photocatalyst. Section 2.2). *In-situ* XAS collected at the Ni K-edge for the reduction and reoxidation of 0.5 wt.% NiO/P25 TiO_2 precursor is shown in Fig. 3, along with reference data for Ni foil and NiO. The XANES spectrum of NiO shows the intense absorption at ~8350 eV, which is characteristic of an octahedral NiO_6 coordination [73]. The Ni K-edge XANES spectrum for the 0.5 wt.% NiO/P25 TiO_2 photocatalyst precursor heated to 400 °C similarly showed a strong absorption peak at ~8350 eV, confirming the presence of NiO (at Time = 0). Following introduction of 1 vol.% H_2 into the sample chamber, a complete reduction of the supported NiO to metallic nickel occurred, evidenced by the disappearance of the 8350 eV feature and the appearance of a distinct shoulder at lower photon energies typical for metallic Ni (the spectrum obtained after H_2 treatment at 400 °C was near identical to that of the metallic Ni reference foil). Cycling between an oxygen-containing atmosphere and a hydrogen-containing atmosphere at 400 °C resulted in either NiO or Ni^0 being present on the P25 TiO_2 surface (Fig. 3), respectively. Finally, the reduced sample was cooled from 400 °C to room temperature under a 1 vol.% H_2 atmosphere, and then exposed to a 1 vol.% O_2 atmosphere. No reoxidation of Ni^0 to NiO occurred, even after several hours. This supports our earlier statement above that the reoxidation of supported metallic nickel nanoparticles on TiO_2 is very slow at room temperature (likely year timescales for even partial reoxidation). Fig. 4 shows the mole fractions of Ni and NiO present as a function of time during the reduction and oxidation steps, determined from the Ni K-edge XANES spectra of Fig. 4. Note that at 400 °C, the oxidation of Ni^0 to NiO is rapid (~ 12 min) compared to the reduction of NiO to Ni^0 (62-69 min).

Corresponding R-space plots obtained from both displayed characteristic peaks at 1.65 Å and 2.6 Å, readily assigned to Ni-O and Ni-Ni distances in NiO, respectively [73, 74]. Following H_2 reduction at 400 °C, these two features disappeared and were replaced by an intense peak at 2.1 Å corresponding to Ni-Ni in metallic nickel with *fcc* symmetry based on additional signals at ~4-6 Å which confirm long range order (Fig. 5) [75, 76]. The XANES and

EXAFS data thus provide strong evidence that metallic Ni is the dominant (and perhaps only) surface species on the TiO_2 support after the H_2 reduction treatment (a result supported by the HRTEM and UV-vis data presented in Fig. 1 and 2, respectively).

Metal co-catalysts (e.g. Ni or Au) are proposed to enhance the photocatalytic activity of TiO_2 for H_2 production under UV excitation by accepting photoexcited electrons from conduction band of TiO_2 and serving as cathodic sites for H_2 evolution [4, 6, 8-11, 14, 17, 19, 25, 28, 49-52, 63]. Photoluminescence spectra collected in air for P25 TiO_2, 0.5 wt.% Ni/P25 TiO_2 and 2 wt.% Au/P25 TiO_2 are shown in Fig. 6, and provide direct evidence for suppression of electron-hole pair recombination in the P25 TiO_2 support in the presence of the added co-catalysts. Following UV excitation, P25 TiO_2 gave a very intense and broad photoluminescence signal centred around 390 nm, which contains contributions from direct and indirect band gap transitions (radiative de-excitation) in anatase and rutile, though mainly the former since anatase is the dominant TiO_2 polymorph in P25 TiO_2 [77]. The high intensity of the photoluminescence signal observed for P25 TiO_2 indicates rapid electron-hole pair recombination occurs following UV excitation. Following deposition of Ni or Au on P25 TiO_2, the photoluminescence signal observed was weaker, confirming that Ni or Au effectively suppresses electron-hole pair recombination in TiO_2 by create a rectifying Schottky junction, since the Fermi level of supported Ni nanoparticles and 5 nm Au nanoparticles is -0.23 V and -0.27 V versus NHE, respectively. The intense photoluminescence signal indicates rapid electron-hole pair recombination following UV excitation. Following deposition of Ni or Au nanoparticles on P25 TiO_2, the photoluminescence signal observed was much weaker, confirming that Ni or Au effectively suppresses electron-hole pair recombination in TiO_2 by creating a rectifying Schottky junction with TiO_2. This result is consistent with expectations, since the Fermi levels of supported Ni nanoparticles and 5 nm Au nanoparticles are located at -0.23 V and -0.27 V versus NHE (cf. the conduction band levels of anatase and rutile are located at -0.5 and -0.7 V versus NHE).

3.2. Effect of alcohol concentration on photocatalytic hydrogen production rates

The photocatalytic performance of the 0.5 wt.% Ni/TiO_2 and 2 wt.% Au/TiO_2 photocatalysts were evaluated in methanol-water, ethanol-water, ethylene glycol-water and glycerol water mixtures at alcohol concentrations ranging from 0-100 vol.% under UV excitation (365 nm, 6.5 mW cm^{-2}). Fig. 7(a)-(d) shows plots of H_2 production versus time for the 0.5 wt.% Ni/P25 TiO_2 photocatalyst in the 4 different alcohol-water mixtures. In all alcohol-water systems, the

H_2 evolution with time was linear confirming that the photocatalyst was stable under the testing condition. Further, there was no induction period before the H_2 evolution commenced, consistent with metallic nickel nanoparticles being the active co-catalyst species for H_2 evolution (Ni^0 was the only surface species at the commencement of the experiment and after the experiment, evidenced by UV-Vis spectroscopy and TEM analyses on as-synthesized and post reaction catalysts). Hydrogen production rates determined from Fig. 7 are summarized in Fig. 8 and Table S1-4. Fig. 8 shows that H_2 production rates for the 0.5 wt.% Ni/P25 TiO_2 photocatalyst were highly dependent on the alcohol concentration, with the optimum concentration for methanol, ethanol, ethylene glycol and glycerol being 40, 95, 20 and 10 vol.%, respectively. H_2 production rates at the optima were 31.1, 24.3, 24.6 and 26.0 mmol g^{-1} h^{-1}, respectively. Corresponding plots of H_2 production versus time for the 2 wt.% Au/P25 TiO_2 photocatalyst are shown in Fig. S2, with the H_2 production rates extracted from Fig. S2 plotted in Fig. 9 and listed Table S1-4. The data for the 2 wt.% Au/P25 TiO_2 photocatalyst was very similar to that collected for the 0.5 wt.% Ni/P25 TiO_2 photocatalyst in the different alcohol-water systems, showing similar optimum alcohol concentrations (for methanol, ethanol, ethylene glycol and glycerol, the optimum alcohol concentration for the Au/P25 TiO_2 photocatalyst was 40, 80, 20 and 15 vol.%, respectively). H_2 production rates at the optima were 29.7, 32.4, 26.4 and 32.7 mmol g^{-1} h^{-1}, respectively. Comparing Fig. 8 and Fig. 9, it can be seen that the 0.5 wt.% Ni/P25 TiO_2 photocatalyst displayed superior performance to the 2 wt.% Au/P25 TiO_2 photocatalyst in methanol-water mixtures, whereas the latter generally demonstrated superior performance in the other alcohol-water mixtures (except at ethanol concentrations < 10 vol.% where Ni/P25 TiO_2 had a slight advantage). However, the main finding of this study is that for all four alcohol-water systems studied, the same general pattern of H_2 production versus alcohol concentration was observed for both the 0.5 wt.% Ni/P25 TiO_2 and 2 wt.% Au/P25 TiO_2 photocatalyst.

The shift in the optimum alcohol concentration for H_2 production with alcohol type warrants further discussion. Table 2 shows redox equations for methanol, ethanol, ethylene glycol and glycerol reforming, as well as calculated standard oxidation potentials (versus NHE) calculated from the Gibbs free energy change for the reforming reactions. If we consider in the first instance only methanol, ethylene glycol and glycerol (i.e. alcohols with a O/C ratio of 1), then the molar ratio H_2O:alcohol required for the reforming reaction are 1:1, 2:1 and 3:1 respectively. Accordingly, it is intuitive that methanol reforming should occur at a higher water concentration than ethylene glycol reforming, with the reforming of the latter occurring at a higher water concentration than glycerol reforming. Indeed, that is the exact trend seen in the

photocatalytic data of Fig. 8 and Fig. 9, with the optimum concentration for H_2 production being 40 vol.% in methanol-water mixtures (at this concentration the molar ratio H_2O:methanol = 3.4), at 20 vol.% in ethylene glycol-water systems (at this concentration the molar ratio H_2O: ethylene glycol = 12.5 and at ~10-15 vol.% in glycerol-water systems (at these concentrations the molar ratio H_2O:glycerol = ~30). It should be noted at this point that under the conditions of our experiments, H_2 is produced by both alcohol photoreforming and water splitting (in the absence of added alcohol, H_2 production rates > 1 mmol g^{-1} h^{-1} were observed for both the 0.5 wt.% Ni/P25 TiO_2 and 2 wt.% Au/P25 TiO_2 photocatalysts in pure water under UV). Even higher rates of water splitting are expected to occur in the presence of the alcohol sacrificial agents due to the significantly improved charge separation in the TiO_2. In part, this co-existence of water splitting and alcohol photoreforming explains why the optimum alcohol concentration for each alcohol-water system differed somewhat from the theoretical molar H_2O:alcohol ratios predicted for methanol, ethylene glycol and glycerol reforming (Table 2). Another important, though generally not appreciated factor that likely influenced the optimum alcohol concentration of the ethylene glycol-water and glycerol-water systems was solution viscosity. At high concentrations, aqueous solutions of ethylene glycol and especially glycerol are very viscous, which has obvious implications for photoreactions in terms of transport of reactants and products to and from, respectively, the photocatalyst surface. At 30 °C, viscosities of methanol, ethanol, ethylene glycol, glycerol and water are 0.659, 1.280, 12.437 and 624 centipoise (cP) , respectively [78, 79]. In Fig. S3, H_2 production rates for the 0.5 wt.% Ni/P25 TiO_2 photocatalyst were plotted against solution viscosity for each alcohol-water system. Corresponding data for the 2 wt.% Au/P25 TiO_2 photocatalyst is plotted in Fig. S4. In the case of ethylene glycol-water and glycerol-water mixtures, H_2 production rates decreased very sharply with increasing viscosity (i.e. increasing alcohol concentration). For the methanol-water and ethanol-water systems, the viscosity change over the whole range of concentrations tested (0-100 vol.%) was 1-2 orders of magnitude smaller than that of the ethylene glycol-water and glycerol-water systems, and hence solution viscosity would have a much lesser impact on H_2 production rates. Finally, it is apparent from Fig. 8 and Fig. 9 that the optimum concentration for ethanol photoreforming (80-95 vol.% depending on the photocatalyst) was much higher than them optimal concentrations determined for the other alcohols. Whilst the theoretical molar ratio H_2O:ethanol for ethanol reforming is 3:1, the lower O/C ratio of 0.5 and the presence of the ethyl group (not present for any of the other alcohols) clearly have an impact on the optimum ethanol concentration. Although a detailed analysis of the other was not performed here (i.e. products other than H_2), it is reasonable to assume that much of the H_2

produced during ethanol photoreactions over the 0.5 wt.% Ni/P25 TiO_2 and 2 wt.% Au/P25 TiO_2 photocatalysts originated from the partial oxidation of ethanol to acetaldehyde (i.e. $CH_3CH_2OH + 2h^+ \rightarrow CH_3CHO + 2H^+$ followed by $2H^+ + 2e^- \rightarrow H_2$) instead of the full photoreforming reaction ($CH_3CH_2OH + 3H_2O + 12h^+ \rightarrow 2CO_2 + 12H^+$ followed by $12H^+ + 12e^- \rightarrow 6H_2$). This would explain why the optimum ethanol concentration was very high, since the partial oxidation route produces H_2 but does not consume H_2O. Cleavage of the C-C bond in ethanol or acetaldehyde or acetates (formed via $CH_3CHO + 2h^+ + H_2O \rightarrow CH_3COOH + 2H^+$) is possibly the rate limiting step in the full ethanol photoreforming reaction. Ethylene glycol and glycerol also contain C-C bonds, though each carbon atom in these alcohol is also bonded to oxygen, making the stepwise oxidation of the alcohol to the aldehyde and eventually to CO_2 thermodynamically easier though the mechanisms involved are complex. Ethylene glycol is first oxidised to glycolaldehyde ($HOCH_2CH_2OH + 2h^+ \rightarrow HOCH_2CHO + 2H^+$), glycolaldehyde to glyoxal ($HOCH_2CHO + 2h^+ \rightarrow HOCCOH + 2H^+$), glyoxal to glycolic acid ($HOCCOH + H_2O \rightarrow HOCOCH_2OH$), glycolic acid to oxalic acid ($HOCOCH_2OH + 4h^+ + H_2O \rightarrow HOOCCOOH + 4H^+$) and finally oxalic acid to CO_2 ($HOOCCOOH + 2h^+ \rightarrow 2CO_2 + 2H^+$) [80, 81]. For glycerol-water mixtures, the mechanism is still under investigation, but the major photocatalytic processes involved are thought to be the oxidation of glycerol to glycolaldehyde and formic acid ($HOCH_2CH(OH)CH_2OH + H_2O + 4h^+ \rightarrow HOCH_2CHO + HCOOH + 4H^+$) [82] and the secondary oxidation of glycolaldehyde to formic acid and formaldehyde ($HOCH_2CHO + H_2O + 4h^+ \rightarrow HCOOH + HCHO + 4H^+$) followed by the simple photocatalytic oxidation of formic acid and formaldehyde to CO_2 [82].

3.3. Effect of alcohol structure on photocatalytic hydrogen production rates

Following the detailed examination of the influence of alcohol concentration on photocatalytic hydrogen production rates, attention was subsequently directed towards the effect of alcohol structure on H_2 production rates for both the 0.5 wt.% Ni/P25 TiO_2 and 2 wt.% Au/P25 TiO_2 photocatalysts. To negate the impact of solution viscosity on H_2 production rates, we selected a fixed alcohol concentration of 10 vol.% to compare the different alcohols, at which concentration all of the aqueous alcohol solutions had a similar viscosity (1-2 centipoise).

Table 3 shows H_2 production rates determined for the 0.5 wt.% Ni/P25 TiO_2 and 2 wt.% Au/P25 TiO_2 photocatalysts in 10 vol.% methanol-water, ethanol-water, ethylene glycol-water and glycerol-water mixtures (corresponding data collected for the same photocatalysts at 80

vol.% alcohol is also tabulated). The data for both photocatalysts reveals the same general trend, with H_2 production rates decreasing in the order glycerol > ethylene glycol > methanol > ethanol. The 0.5 wt.% Ni/P25 TiO_2 photocatalyst afforded rates of 26.0, 21.4, 15.7 and 11.6 mmol g^{-1} h^{-1} in 10 vol.% glycerol, ethylene glycol, methanol and ethanol, respectively. The 2 wt.% Au/P25 TiO_2 photocatalyst afforded corresponding rates of 30.3, 25.8, 16.9 and 10.0 mmol g^{-1} h^{-1}, respectively. In order to understand the trend seen in the H_2 production rates, the structure and physical properties of the four different alcohols need to be considered. Table 4 summarises key physical properties of the four alcohols studied in this work. In Fig. 10 and 11 we have plotted H_2 production rates against specific properties of the alcohols, namely the number of alpha hydrogens on the alcohol, the number of OH groups on the alcohol, alcohol polarity and finally exp($-\Delta E^o$), where $\Delta E^o = E^o_{VB(TiO2)} - E^o_{ox}$ (the justification for which is discussed below). In all cases, reasonable linear correlations can be established between the H_2 production rates and the selected physical properties of the alcohols, with both the 0.5 wt.% Ni/P25 TiO_2 and 2 wt.% Au/P25 TiO_2 photocatalysts showing similar behaviours.

The photoreforming of the alcohols can be represented by the following general equation [48]:

$C_xH_yO_z + (2x - z)H_2O \rightarrow xCO_2 + nH^+ + ne^-$

where x, y and z are the number of carbon, hydrogen and oxygen atoms in alcohol, respectively, and n is the number of protons or electrons liberated. The photoreaction will proceed via the formation of alpha hydroxyl radicals in the aqueous media followed by oxidation to the corresponding aldehyde, which accounts for the importance of α-H atoms on the alcohol to achieving high H_2 production rates [11]. The interaction of lone pairs on the OH groups with unoccupied Ti 3d states is important for the physical adsorption of the alcohols and alpha hydroxyl radicals on the TiO_2 surface (hence the relationship between H_2 production rates and the number of OH groups on the alcohol, in addition to the adsorption strength of the alcohols on TiO_2 decreasing in the order glycerol > ethylene glycol > mono alcohols) (Fig. 10). The dependence of H_2 production rates on alcohol polarity and alcohol oxidation potential are in accord with the findings of Yang et al. for the Pt/TiO_2 system and Al-Azri et al. for Pd/TiO_2, Pt/TiO_2 and Au/TiO_2 system [14, 22]. The standard oxidation potentials (E_{ox}^o) calculated for methanol, ethanol, ethylene glycol and glycerol (Table 2) were 0.016, 0.084, 0.009 and 0.004 V versus NHE, respectively, all significantly lower than the oxidation potential of water (1.23 V versus NHE). Hence, during photocatalysis in alcohol-water systems, the alcohols will be preferentially oxidised, though water will also be oxidised through direct water splitting and

alcohol photo-reforming. Glycerol and ethylene glycol afforded the highest H_2 production rates for Ni/P25 TiO_2 and Au/P25 TiO_2 photocatalysts (Table 3), which can be rationalised in terms of their low oxidation potentials making them the best sacrificial hole scavengers. Considering a simple electron transfer reaction between an electron donor and an electron acceptor (valence band holes in TiO_2 in this case) [83], the experimental rate constant (k_{exp}) for such reactions follows the relation:

$$k_{exp} \propto \exp^{-(E^{o}_{VB(TiO_2)} - E^{o}_{ox})/RT}$$

where $E^{o}_{VB(TiO_2)}$ and E^{o}_{ox} are the valence band potential of TiO_2 (2.7 V for anatase) and the oxidation potential of the donor (alcohol or water), respectively. If electron transfer from the alcohols or water to TiO_2 was the overall rate limiting step in photocatalytic H_2 production over Ni/TiO_2 and Au/TiO_2 surfaces, then H_2 production rates could be expected to correlate with $\exp^{-(E^{o}_{VB(TiO2)} - E^{o}_{ox})}$. Fig. 11(b) confirms a linear relationship between the H_2 production rates and $\exp(-\Delta E^{o})$ for both the Ni/TiO_2 and Au/TiO_2 photocatalysts (data for ethanol was excluded since it did not have a O:C ratio = 1 like the other alcohols).

3.4. Synergistic role of anatase-rutile heterokunctions in H_2 production over the Ni/P25 TiO_2 photocatlyst

Previous studies of P25 TiO_2 photocatalysts have demonstrated the critical role of anatase-rutile heterojunctions in promoting rates of aqueous dye degradation and also photocatalytic H_2 production [68, 84]. Under UV excitation, both anatase and rutile generate charge carriers (electron-hole pairs). Rutile is a direct band gap semiconductor whereas anatase is an indirect band gap semiconductor, thus rates of electron-hole pair generation (and also recombination) are much faster in rutile than in anatase. By fusing anatase and rutile nanoparticles, as is the case in P25 TiO_2, conduction band electrons in rutile can migrate into the conduction band of anatase (possible since the conduction band of rutile at -0.2 V is more negative versus NHE than that of anatase), whilst valence band holes in anatase migrate into the valence band of rutile (again possible since the VB of anatase is +0.4 V more positive versus NHE than that of rutile). The net effect of the anatase-rutile heterojunctions in P25 is a significant improvement in charge separation following photoexcitation which increases the number of charge carriers (holes and electrons) reaching the photocatalyst surface and participating in photoreactions. For this reason, P25 TiO_2-based photocatalysts generally display superior photocatalytic

activities to single polymorph TiO_2 photocatalysts (e.g. pure anatase, brookite or rutile). To determine the extent to which anatase-rutile heterojunctions promoted photocatalytic H_2 production in the 0.5 wt.% Ni/P25 TiO_2 system, we prepared two further 0.5 wt.% Ni/TiO_2 photocatalysts using anatase and rutile nanoparticles isolated from P25 TiO_2 by selective chemical dissolution (see methods section). Fig. S5 shows XRD patterns for the anatase and rutile nanoparticles isolated by this approach, which were almost pure phase. From these isolated anatase and rutile nanoparticles, a 0.5 wt.% Ni/anatase photocatalyst and a 0.5 wt.% Ni/(85% anatase + 15% rutile) photocatalyst were prepared, and their performance evaluated against the 0.5 wt.% Ni/P25 TiO_2 photocatalyst for H_2 production in 10 vol.% alcohol-water mixtures under UV excitation. Results are shown in Fig. 12 and Table 5. Fig. 12(a)-(c) show that all photocatalysts were stable under the testing conditions, evidence by linear H_2 production with time. Also, all 3 photocatalysts showed the same general trend in H_2 production rates, with rates decreasing in the familiar order glycerol > ethylene glycol > methanol > ethanol (Table 5 and Fig. 12(d)). However, in all alcohol-water systems tested, H_2 production rates were significantly higher for the 0.5 wt.% Ni/P25 TiO_2 photocatalyst than other two catalysts, emphasizing the importance of interfacial electron and hole migration at the anatase-rutile interface to the high photoactivity of P25 TiO_2. Such migration is negligible in the Ni/anatase and Ni/(85% anatase + 15% rutile) photocatalysts.

Currently we are attempting to quantify other products formed during the H_2 production tests in order to gain a better understanding the photoreaction mechanism(s) and also to ascertain the relative contributions water splitting and alcohol photoreforming to the H_2 yields reported here.

3.5. Schematic of photocatalytic H_2 production in the Ni/P25 TiO_2 (or Au/P25 TiO_2) system

Fig. 13 shows a schematic energy diagram of the key processes leading to H_2 evolution over the Ni/P25 TiO_2 photocatalysts [28, 37, 38]. Photoexcitation under UV generates electron hole pairs in both TiO_2 polymorphs [85, 86]. , with electrons accumulatting in the conduction band of anatase and holes in the valence band of rutile due to the favorable offsets of their respective valence and conduction bands. The valence band holes migrate to the surface of TiO_2 nanoparticles (especially to the surface of rutile) and oxidize alcohols and to a lesser extent water to generate H^+, whilst electrons in the conduction band of the TiO_2 nanoparticles (mainly in anatase) migrate onto Ni^0 nanoparticles (or Au^0 nanoparticles) which serve cathodic sites for

H_2 evolution ($2H^+ + 2e^- \rightarrow H_2$). The appropriate Fermi level positions of Ni^0 (or Au^0) together with its high work function create an effective Schottky barrier preventing the unwanted migration of electrons back into the conduction band of TiO_2.

4. Conclusion

Ni/P25 TiO_2 and Au/P25 TiO_2 photocatalysts exhibit very similar photocatalytic activity for H_2 production in alcohol-water mixtures under UV excitation. For both photocatalyst systems and a fixed alcohol concentration of 10 vol.%, H_2 production rates were found to decrease in the order glycerol > ethylene glycol > methanol > ethanol. Reasonable linear correlations could be established between the H_2 production rates and specific properties of the alcohol, such as number of OH groups, polarity and the standard oxidation potential of the alcohol. H_2 production rates were strongly dependent on the alcohol concentration, with the optimum alcohol concentration determined to be 10-15 vol.% for glycerol, 20 vol.% for ethylene glycol, 40 vol.% for methanol and 80-95 vol.% for ethanol. For the ethylene glycol-water and glycerol-water systems, the solution viscosity increased marked with concentration above 10-20 vol.%, which detrimentally impacted photocatalytic production rates. Anatase-rutile heterojunctions in the P25 TiO_2 support were shown to enhance photocatalytic H_2 production, by allowing electron and hole transfer between the polymorphs which increased the availability of valence band holes for alcohol and water oxidation and conduction band electrons for subsequent proton reduction to H_2 on supported Ni^0 or Au^0 sites. On account of the similarity of the photocatalytic data reported here for the Ni/P25 TiO_2 and Au/P25 TiO_2 photocatalysts (in fact Ni/P25 TiO_2 was superior in all methanol-water mixtures and ethanol-water mixtures at concentrations < 10 vol.%), it can be concluded that Ni/TiO_2 photocatalysts are very promising low cost alternatives to noble metal-based photocatalysts for solar H_2 production in alcohol-water mixtures.

Acknowledgements

Wan-Ting Chen and Andrew Chan thank the Energy Education Trust of New Zealand for the award of Doctoral Scholarships and AINSE Ltd for providing financial assistance (Postgraduate Research Awards). Additional funding support from the University of Auckland FRDF fund, New Zealand Synchrotron Group Ltd and the MacDiarmid Institute for Advanced Materials and Nanotechnology is gratefully acknowledged. Geoff Waterhouse thanks the Japan Society for the Promotion of Science (JSPS) for award of a

JSPS Fellowship to work in Japan (S13179). The authors thank Dr. Toshiaki Ina (SPring-8) for his assistance with the collection and processing of the Ni K-edge EXAFS data. The synchrotron radiation experiments were performed at the BL01B1 (XAFS) of SPring-8 with the approval of the Japan Synchrotron Radiation Research Institute (JASRI) (Proposal No. 2014B1065).

References

[1] K. Mazloomi, C. Gomes, Renewable and Sustainable Energy Reviews, 16 (2012) 3024-3033.
[2] N. Armaroli, V. Balzani, ChemSusChem, 4 (2011) 21-36.
[3] J. Ran, J. Zhang, J. Yu, M. Jaroniec, S.Z. Qiao, Chem. Soc. Rev., 43 (2014) 7787-7812.
[4] L. Barelli, G. Bidini, F. Gallorini, S. Servili, Energy, 33 (2008) 554-570.
[5] J.P. Van Hook, Catalysis Reviews—Science and Engineering, 21 (1980) 1-51.
[6] A. Kudo, Y. Miseki, Chem. Soc. Rev., 38 (2009) 253-278.
[7] K. Maeda, K. Domen, The Journal of Physical Chemistry Letters, 1 (2010) 2655-2661.
[8] X. Chen, S. Shen, L. Guo, S.S. Mao, Chem. Rev., 110 (2010) 6503-6570.
[9] I. Dincer, Int. J. Hydrogen Energy, 37 (2012) 1954-1971.
[10] H. Ahmad, S. Kamarudin, L. Minggu, M. Kassim, Renewable and Sustainable Energy Reviews, 43 (2015) 599-610.
[11] M. Bowker, C. Morton, J. Kennedy, H. Bahruji, J. Greves, W. Jones, P.R. Davies, C. Brookes, P.P. Wells, N. Dimitratos, J. Catal., 310 (2014) 10-15.
[12] M. Bowker, Catal. Lett., 142 (2012) 923-929.
[13] H. Bahruji, M. Bowker, P.R. Davies, J. Kennedy, D.J. Morgan, Int. J. Hydrogen Energy, 40 (2015) 1465-1471.
[14] Y.Z. Yang, C.H. Chang, H. Idriss, Applied Catalysis B: Environmental, 67 (2006) 217-222.
[15] R.I. Bickley, T. Gonzalez-Carreno, J.S. Lees, L. Palmisano, R.J. Tilley, J. Solid State Chem., 92 (1991) 178-190.
[16] M. Ni, M.K. Leung, D.Y. Leung, K. Sumathy, Renewable and Sustainable Energy Reviews, 11 (2007) 401-425.
[17] A. Gallo, T. Montini, M. Marelli, A. Minguzzi, V. Gombac, R. Psaro, P. Fornasiero, V. Dal Santo, ChemSusChem, 5 (2012) 1800-1811.
[18] V. Jovic, Z.H.N. Al-Azri, W.-T. Chen, D. Sun-Waterhouse, H. Idriss, G.I.N. Waterhouse, Topics in Catalysis, 56 (2013) 1139-1151.
[19] G.R. Bamwenda, S. Tsubota, T. Nakamura, M. Haruta, Journal of Photochemistry and Photobiology A: Chemistry, 89 (1995) 177-189.
[20] M. Bowker, C. Morton, J. Kennedy, H. Bahruji, J. Greves, W. Jones, P.R. Davies, C. Brookes, P. Wells, N. Dimitratos, Journal of Catalysis, 310 (2014) 10-15.
[21] A. Wahab, S. Bashir, Y. Al-Salik, H. Idriss, Applied Petrochemical Research, 4 (2014) 55-62.
[22] Z.H.N. Al-Azri, W.-T. Chen, A. Chan, V. Jovic, T. Ina, H. Idriss, G.I.N. Waterhouse, J. Catal., 329 (2015) 355-367.
[23] Y. Li, B. Wang, S. Liu, X. Duan, Z. Hu, Appl. Surf. Sci., 324 (2015) 736-744.
[24] J. Bandara, C. Udawatta, C. Rajapakse, Photochemical & Photobiological Sciences, 4 (2005) 857-861.

[25] W.-T. Chen, V. Jovic, D. Sun-Waterhouse, H. Idriss, G.I.N. Waterhouse, Int. J. Hydrogen Energy, 38 (2013) 15036-15048.
[26] H.L. Skriver, N. Rosengaard, Physical Review B, 46 (1992) 7157.
[27] M. Jaksic, J. New Mater. Electrochem. Syst., 3 (2000) 153-168.
[28] W.-T. Chen, A. Chan, D. Sun-Waterhouse, T. Moriga, H. Idriss, G.I.N. Waterhouse, J. Catal., 326 (2015) 43-53.
[29] L. Fan, J. Long, Q. Gu, H. Huang, H. Lin, X. Wang, Journal of Catalysis, 320 (2014) 147-159.
[30] T. Sreethawong, Y. Suzuki, S. Yoshikawa, Int. J. Hydrogen Energy, 30 (2005) 1053-1062.
[31] D. Jing, Y. Zhang, L. Guo, Chem. Phys. Lett., 415 (2005) 74-78.
[32] A. Kudo, K. Domen, K.-i. Maruya, T. Onishi, Chem. Phys. Lett., 133 (1987) 517-519.
[33] E.P. Melián, M.N. Suárez, T. Jardiel, J.M.D. Rodríguez, A.C. Caballero, J. Araña, D.G. Calatayud, O.G. Díaz, Applied Catalysis B: Environmental, 152–153 (2014) 192-201.
[34] L. Li, B. Cheng, Y. Wang, J. Yu, J. Colloid Interface Sci., 449 (2015) 115-121.
[35] R. Liu, H. Yoshida, S.-i. Fujita, M. Arai, Applied Catalysis B: Environmental, 144 (2014) 41-45.
[36] Y. Shen, A.C. Lua, RSC Advances, 4 (2014) 42159-42167.
[37] J. Yu, Y. Hai, B. Cheng, The Journal of Physical Chemistry C, 115 (2011) 4953-4958.
[38] W. Wang, S. Liu, L. Nie, B. Cheng, J. Yu, PCCP, 15 (2013) 12033-12039.
[39] P.D. Tran, L. Xi, S.K. Batabyal, L.H. Wong, J. Barber, J.S. Chye Loo, PCCP, 14 (2012) 11596-11599.
[40] L. Zhang, Q. Liu, T. Aoki, P.A. Crozier, The Journal of Physical Chemistry C, 119 (2015) 7207-7214.
[41] E. Cui, G. Lu, Int. J. Hydrogen Energy, 39 (2014) 8959-8968.
[42] M.D. Irwin, D.B. Buchholz, A.W. Hains, R.P. Chang, T.J. Marks, Proceedings of the National Academy of Sciences, 105 (2008) 2783-2787.
[43] L. Chu, M. Li, P. Cui, Y. Jiang, Z. Wan, S. Dou, Energy and Environment Focus, 3 (2014) 371-374.
[44] G.I.N. Waterhouse, M. Murdoch, J. Llorca, H. Idriss, International Journal of Nanotechnology, 9 (2012) 113-120.
[45] M. Murdoch, G.I.N. Waterhouse, M.A. Nadeem, J.B. Metson, M.A. Keane, R.F. Howe, J. Llorca, H. Idriss, Nature Chemistry, 3 (2011) 489-492.
[46] B.S. Kwak, J. Chae, J. Kim, M. Kang, Bull. Korean Chem. Soc., 30 (2009) 1047-1053.
[47] N.H. Tran, G.K. Kannangara, Chem. Soc. Rev., 42 (2013) 9454-9479.
[48] K. Shimura, H. Yoshida, Energy & Environmental Science, 4 (2011) 2467-2481.
[49] H. Bahruji, M. Bowker, P.R. Davies, F. Pedrono, Applied Catalysis B: Environmental, 107 (2011) 205-209.
[50] M. Bowker, H. Bahruji, J. Kennedy, W. Jones, G. Hartley, C. Morton, Catal. Lett., 1-6.
[51] J. Greaves, L. Al-Mazroai, A. Nuhu, P. Davies, M. Bowker, Gold Bulletin, 39 (2006) 216-219.
[52] V. Jovic, Z.H. Al-Azri, W.-T. Chen, D. Sun-Waterhouse, H. Idriss, G.I.N. Waterhouse, Top. Catal., 56 (2013) 1139-1151.
[53] A. Tanaka, S. Sakaguchi, K. Hashimoto, H. Kominami, Acs Catalysis, 3 (2012) 79-85.

[54] G. Wu, T. Chen, W. Su, G. Zhou, X. Zong, Z. Lei, C. Li, Int. J. Hydrogen Energy, 33 (2008) 1243-1251.
[55] M. Stelmachowski, M. Marchwicka, E. Grabowska, M. Diak, A. Zaleska, Journal of Advanced Oxidation Technologies, 17 (2014) 179-186.
[56] A. Petala, E. Ioannidou, A. Georgaka, K. Bourikas, D.I. Kondarides, Appl. Catal. B, 178 (2015) 201-209.
[57] V.M. Daskalaki, D.I. Kondarides, Catal. Today, 144 (2009) 75-80.
[58] Slamet, D. Tristantini, Valentina, M. Ibadurrohman, International Journal of Energy Research, 37 (2013) 1372-1381.
[59] B. Ahmmad, K. Kanomata, F. Hirose, Int. J. Chem. Mater. Sci. Eng., 8 (2014) 24-29.
[60] K. Lalitha, G. Sadanandam, V.D. Kumari, M. Subrahmanyam, B. Sreedhar, N.Y. Hebalkar, The Journal of Physical Chemistry C, 114 (2010) 22181-22189.
[61] G. Sadanandam, K. Lalitha, V.D. Kumari, M.V. Shankar, M. Subrahmanyam, Int. J. Hydrogen Energy, 38 (2013) 9655-9664.
[62] R. Zanella, S. Giorgio, C.R. Henry, C. Louis, The Journal of Physical Chemistry B, 106 (2002) 7634-7642.
[63] V. Jovic, W.-T. Chen, D. Sun-Waterhouse, M.G. Blackford, H. Idriss, G.I.N. Waterhouse, J. Catal., 305 (2013) 307-317.
[64] L. Yoong, F.K. Chong, B.K. Dutta, Energy, 34 (2009) 1652-1661.
[65] J.T. Richardson, R. Scates, M.V. Twigg, Applied Catalysis A: General, 246 (2003) 137-150.
[66] T. Ohno, K. Sarukawa, M. Matsumura, J. Phys. Chem. B, 105 (2001) 2417-2420.
[67] B. Ohtani, O.O. Prieto-Mahaney, D. Li, R. Abe, J. Photochem. Photobiol. A, 216 (2010) 179-182.
[68] W.-T. Chen, A. Chan, V. Jovic, D. Sun-Waterhouse, K.-i. Murai, H. Idriss, G.I.N. Waterhouse, Top. Catal., 58 (2015) 85-102.
[69] X.-Z. Ding, X.-H. Liu, Y.-Z. He, J. Mater. Sci. Lett., 15 (1996) 1789-1791.
[70] K. Okumura, J. Amano, N. Yasunobu, M. Niwa, The Journal of Physical Chemistry B, 104 (2000) 1050-1057.
[71] S. Brunauer, P.H. Emmett, E. Teller, J. Am. Chem. Soc., 60 (1938) 309-319.
[72] E.P. Barrett, L.G. Joyner, P.P. Halenda, J. Am. Chem. Soc., 73 (1951) 373-380.
[73] L. Fan, J. Long, Q. Gu, H. Huang, H. Lin, X. Wang, J. Catal., 320 (2014) 147-159.
[74] A. Corrias, G. Mountjoy, G. Piccaluga, S. Solinas, The Journal of Physical Chemistry B, 103 (1999) 10081-10086.
[75] V.M. Gonzalez-DelaCruz, J.P. Holgado, R. Pereñíguez, A. Caballero, J. Catal., 257 (2008) 307-314.
[76] H. Kitagawa, N. Ichikuni, H. Okuno, T. Hara, S. Shimazu, Applied Catalysis A: General, 478 (2014) 66-70.
[77] N. Daude, C. Gout, C. Jouanin, Phys. Rev. B, 15 (1977) 3229-3235.
[78] M. Dizechi, E. Marschall, J. Chem. Eng. Data, 27 (1982) 358-363.
[79] M.L. Sheely, Industrial & Engineering Chemistry, 24 (1932) 1060-1064.
[80] H. Yue, Y. Zhao, X. Ma, J. Gong, Chem. Soc. Rev., 41 (2012) 4218-4244.
[81] J. Schnaidt, M. Heinen, Z. Jusys, R.J. Behm, The Journal of Physical Chemistry C, 117 (2013) 12689-12701.
[82] R. Chong, J. Li, X. Zhou, Y. Ma, J. Yang, L. Huang, H. Han, F. Zhang, C. Li, Chem. Commun., 50 (2014) 165-167.

[83] V. Balzani, F. Scandola, Light-Induced and Thermal Electron-Transfer Reactions, in: M. Gratzel (Ed.) Energy Resources through Photochemistry and Catalysis, Academic Press Inc., New York, 1983, pp. 2-48.
[84] V. Jovic, K.E. Smith, H. Idriss, G.I. Waterhouse, ChemSusChem, 8 (2015) 2551-2559.
[85] D.O. Scanlon, C.W. Dunnill, J. Buckeridge, S.A. Shevlin, A.J. Logsdail, S.M. Woodley, C.R.A. Catlow, M.J. Powell, R.G. Palgrave, I.P. Parkin, Nature materials, 12 (2013) 798-801.
[86] S.N. Habisreutinger, L. Schmidt-Mende, J.K. Stolarczyk, Angew. Chem. Int. Ed., 52 (2013) 7372-7408.

Figure Captions:

Figure 1 – (a)-(b) STEM/HAADF images of 0.5 wt.% Ni/P25 TiO_2 photocatalyst with EDX spectra shown as insets; (c)-(e) HRTEM images of 0.5 wt.% Ni/P25 TiO_2 photocatalyst with insets showing lattice fringes and selected area diffraction patterns from supported metallic Ni nanoparticles; (f) TEM image of the 2 wt.% Au/P25 TiO_2 photocatalyst.

Figure 2 – (a) UV-Visible absorbance spectra for P25 TiO_2, 0.63 wt.% NiO/P25, 0.5 wt.% Ni/P25 TiO_2 and 2 wt.% Au/P25 TiO_2 photocatalysts. (b) Corresponding Tauc plots for P25 TiO_2, 0.63 wt.% NiO/P25, 0.5 wt.% Ni/P25 TiO_2 and 2 wt.% Au/P25 TiO_2 photocatalysts.

Figure 3 – *In-situ* Ni K-edge XANES under different conditions for a 0.63 wt.% NiO/P25 TiO_2 photocatalyst subjected to repeated cycles of H_2 reduction and oxidation at 400 ^oC, followed by final cooling of the reduced form to room temperature and then exposure to O_2. Time (in minutes) from the beginning of the experiments is shown on the left.

Figure 4 – Fraction of nickel as metallic Ni or NiO for the 0.63 wt.% NiO/P25 TiO_2 photocatalyst under different treatment conditions, determined from the *in-situ* Ni K-edge EXAFS data in Fig. 3. The coloured vertical dotted lines correspond to individual spectra in Figure 4.

Figure 5 – R-space plots based on Fourier transforms on k^3-weighted *in-situ* Ni K-edge EXAFS oscillations for for a 0.63 wt.% NiO/P25 TiO_2 photocatalyst subjected to repeated cycles of H_2 reduction and oxidation at 400 °C, followed by final cooling of the reduced form to room temperature and then exposure to O_2.

Figure 6 – Photoluminescence spectra for (a) P25 TiO_2; (b) 0.5 wt.% Ni/P25 TiO_2; and (c) 2 wt.% Au/P25 TiO_2 following UV excitation.

Figure 7 – Plots of H_2 production versus time for the 0.5 wt.% Ni/P25 TiO_2 photocatalyst in different alcohol:H_2O mixtures under UV irradiation. (a) methanol; (b) ethanol; (c) ethylene glycol; and (d) glycerol.

Figure 8 – Rates of H_2 production versus alcohol type and alcohol concentration for the 0.5 wt.% Ni/P25 TiO_2 photocatalyst under UV irradiation.

Figure 9 – Rates of H_2 production versus alcohol concentration for the 2 wt.% Au/P25 TiO_2 photocatalyst under UV irradiation.

Figure 10 – H_2 production rates for 0.5 wt.% Ni/P25 TiO_2 and 2 wt.% Au/P25 TiO_2 photocatalyst versus (a) number of α-H on the alcohol; and (b) number of OH groups on the alcohol.

Figure 11 – H_2 production rates for 0.5 wt.% Ni/P25 TiO_2 and 2 wt.% Au/P25 TiO_2 photocatalyst versus (a) alcohol polarity; and (b) alcohol oxidation potential. Data for ethanol was excluded from (b).

Figure 12 – Plots of H_2 production rate versus time for different 0.5 wt.% Ni/TiO_2 photocatalysts in 10 vol.% alcohol-water mixtures under UV irradiation: (a) 0.5 wt.% Ni/P25 TiO2; (b) 0.5 wt.% Ni/anatase isolated from P25 TiO_2; and (c) 0.5 wt.% Ni/(85% anatase + 15 % rutile physical mixture); (d) performance comparison of selected Ni/TiO_2 photocatalysts.

Figure 13 – Schematic illustration showing the important electron transfer processes in the Ni/TiO_2 system leading to H_2 production.

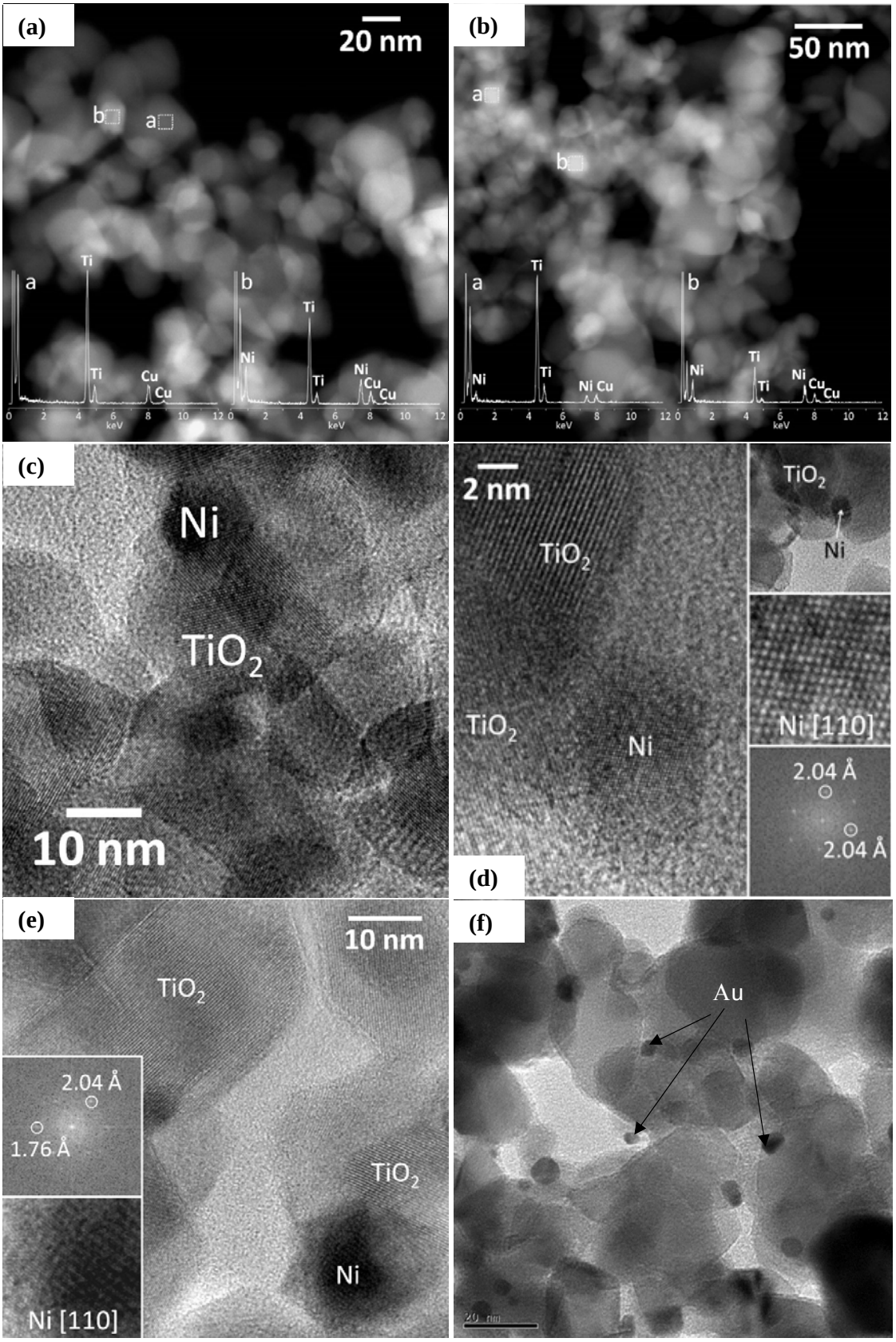
(a)
20 nm
b
a
a
Ti
Ti
Cu
Cu
b
Ni
Ti
Ti
Ni
Cu
Cu
keV
(b)
50 nm
a
b
a
Ni
Ti
Ni Cu
b
Ni
Ti
Ti
Ni
Cu
Cu
keV
(c)
Ni
TiO2
10 nm
2 nm
TiO2
TiO2
Ni
TiO2
Ni
Ni [110]
2.04 Å
2.04 Å
(d)
(e)
10 nm
TiO2
2.04 Å
1.76 Å
TiO2
Ni
Ni [110]
(f)
Au

Fig 1.

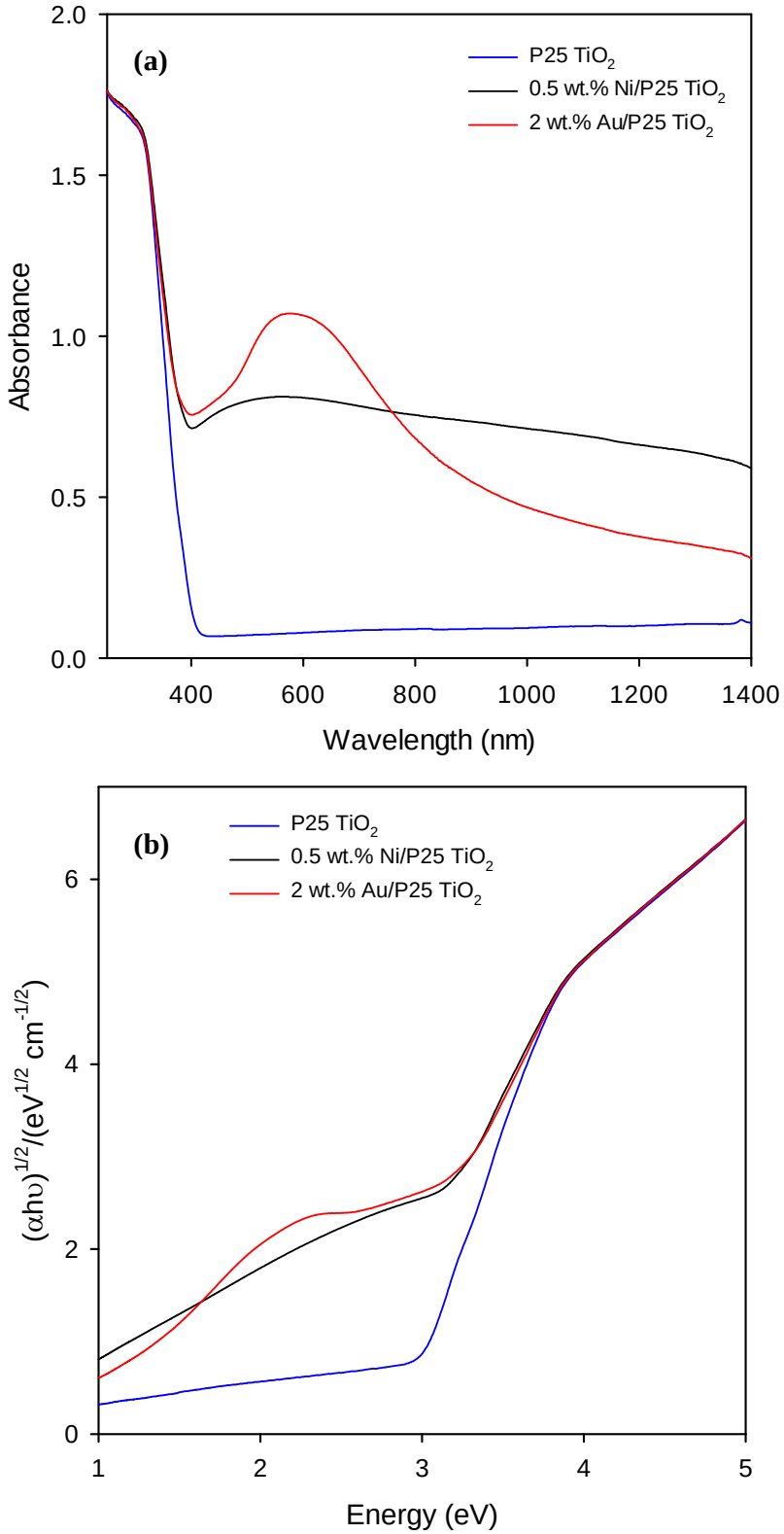
(a)
P25 TiO2
0.5 wt.% Ni/P25 TiO2
2 wt.% Au/P25 TiO2
Absorbance
Wavelength (nm)
2.0
1.5
1.0
0.5
0.0
400
600
800
1000
1200
1400
(b)
P25 TiO2
0.5 wt.% Ni/P25 TiO2
2 wt.% Au/P25 TiO2
(αhυ)1/2/(eV1/2 cm-1/2)
Energy (eV)
6
4
2
0
1
2
3
4
5

Fig. 2

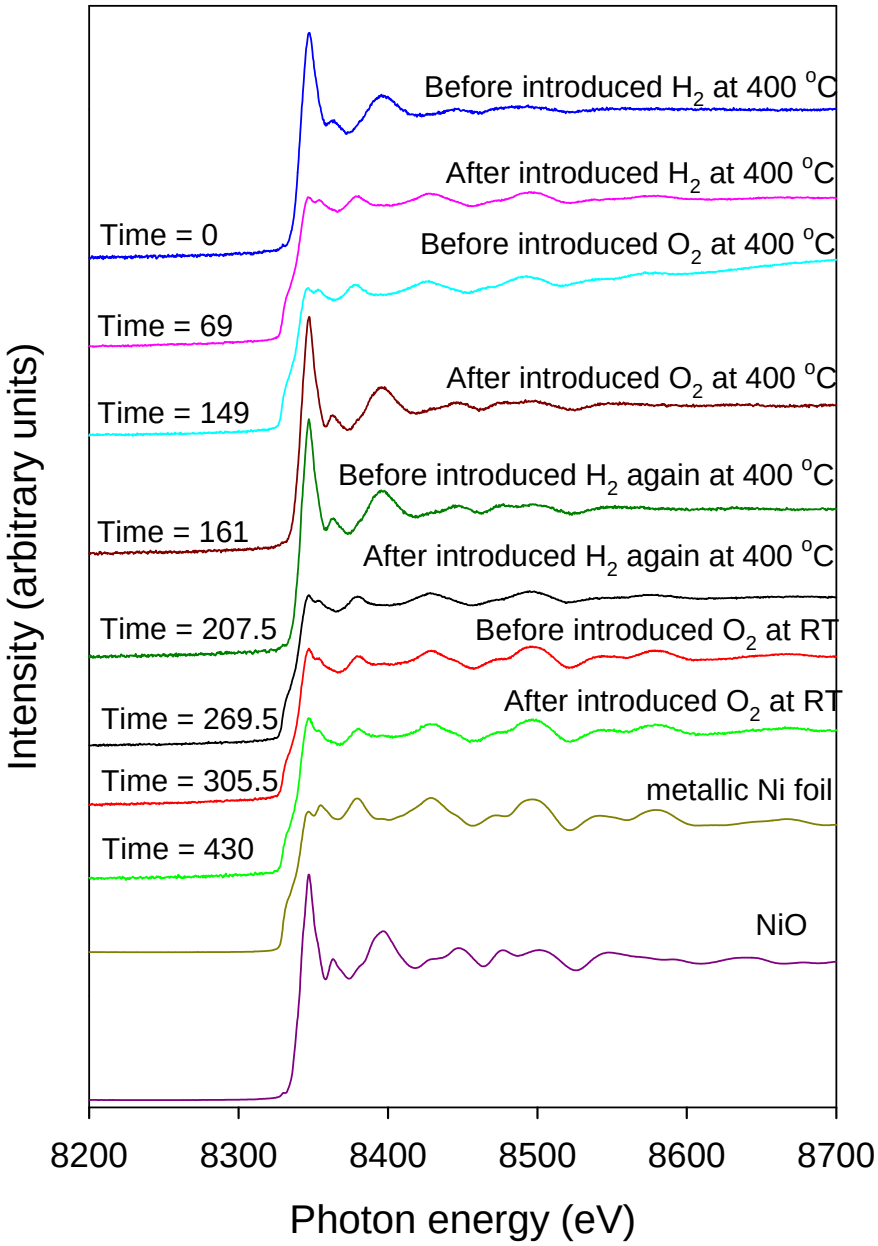
Before introduced H2 at 400 °C
After introduced H2 at 400 °C
Time = 0
Before introduced O2 at 400 °C
Time = 69
After introduced O2 at 400 °C
Time = 149
Before introduced H2 again at 400 °C
Time = 161
After introduced H2 again at 400 °C
Time = 207.5
Before introduced O2 at RT
Time = 269.5
After introduced O2 at RT
Time = 305.5
metallic Ni foil
Time = 430
NiO
Intensity (arbitrary units)
8200
8300
8400
8500
8600
8700
Photon energy (eV)

Fig. 3

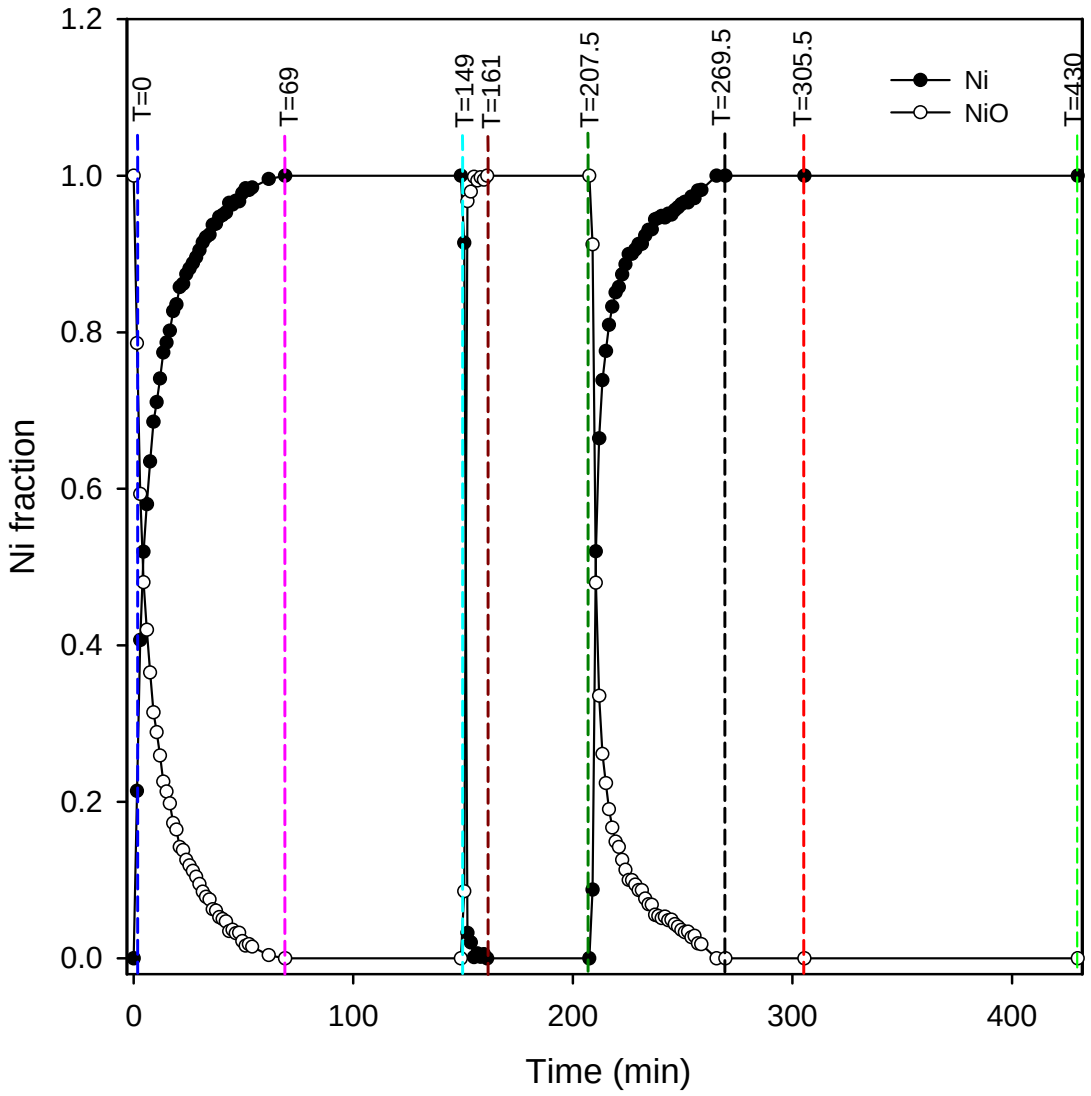
1.2
1.0
0.8
0.6
0.4
0.2
0.0
Ni fraction
0
100
200
300
400
Time (min)
T=0
T=69
T=149
T=161
T=207.5
T=269.5
T=305.5
T=430
Ni
NiO

Fig. 4

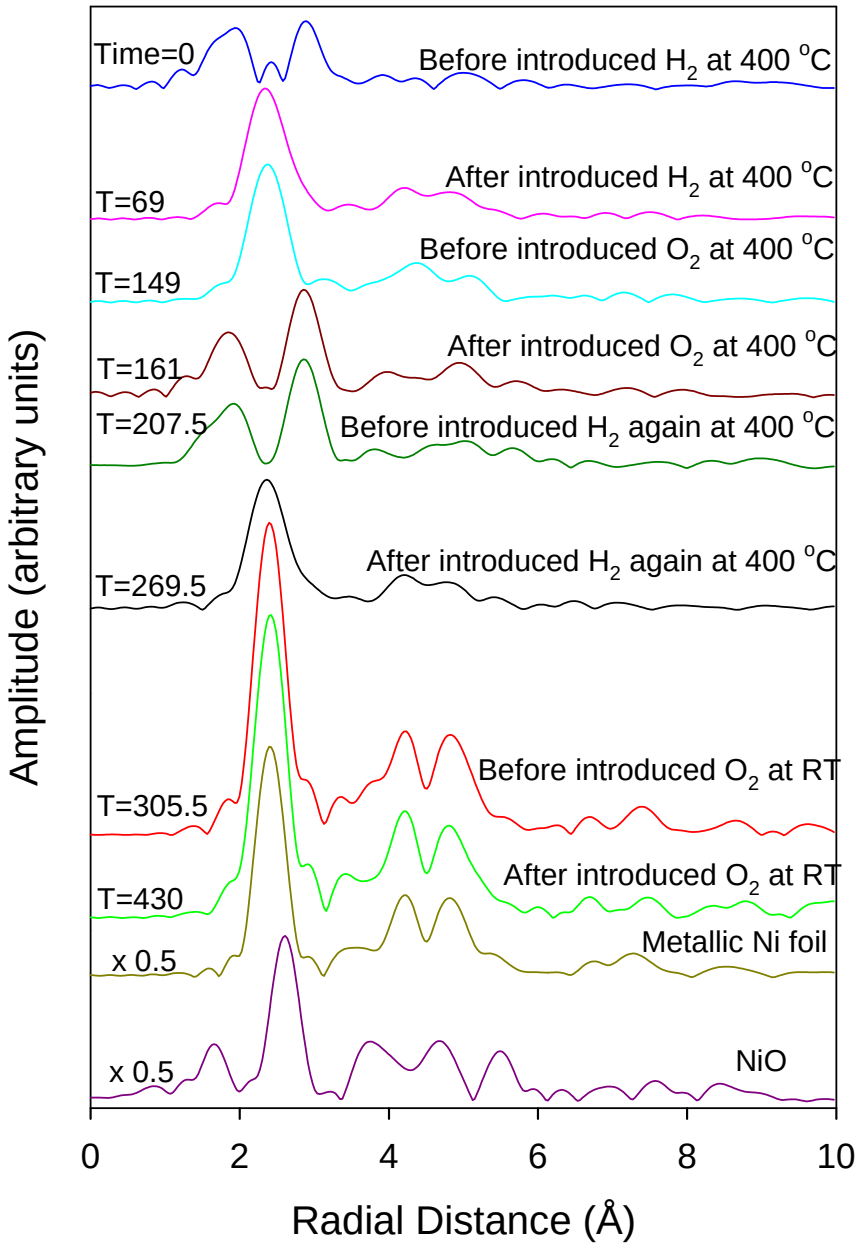
Time=0
Before introduced H2 at 400 oC
T=69
After introduced H2 at 400 oC
T=149
Before introduced O2 at 400 oC
T=161
After introduced O2 at 400 oC
T=207.5
Before introduced H2 again at 400 oC
T=269.5
After introduced H2 again at 400 oC
T=305.5
Before introduced O2 at RT
T=430
After introduced O2 at RT
x 0.5
Metallic Ni foil
x 0.5
NiO
Amplitude (arbitrary units)
0
2
4
6
8
10
Radial Distance (Å)

Fig. 5

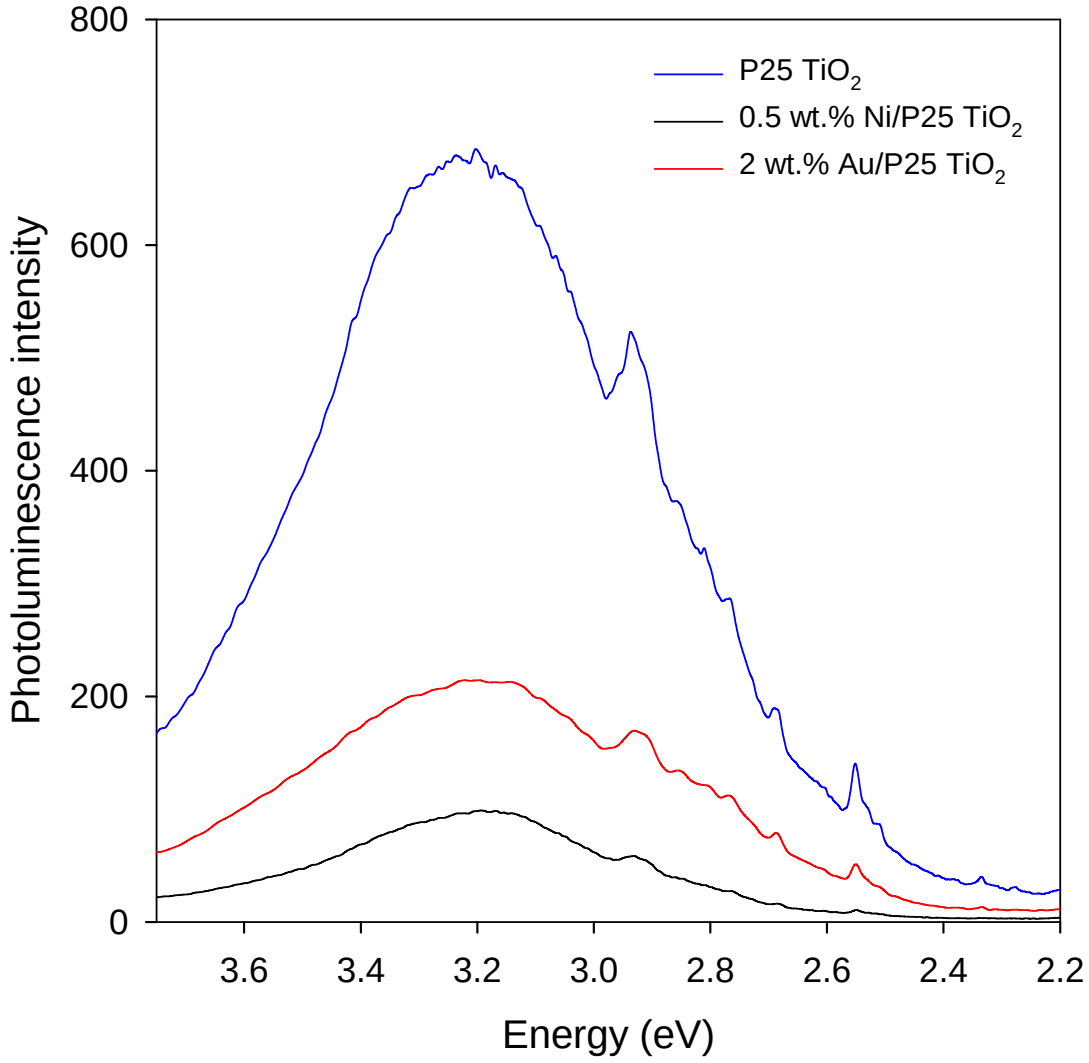
800
600
400
200
0
Photoluminescence intensity
3.6
3.4
3.2
3.0
2.8
2.6
2.4
2.2
Energy (eV)
P25 TiO2
0.5 wt.% Ni/P25 TiO2
2 wt.% Au/P25 TiO2

Fig. 6

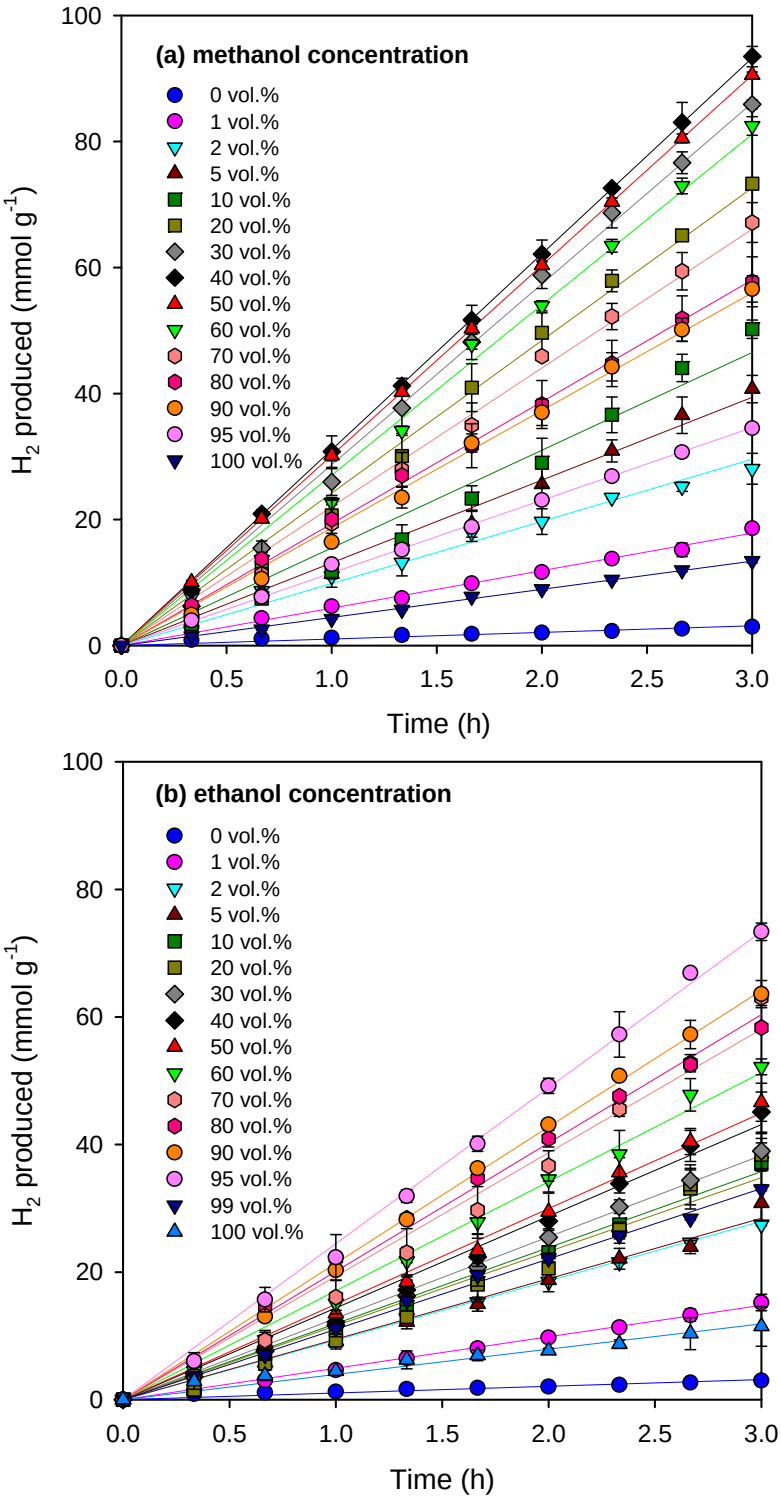
(a) methanol concentration
0 vol.%
1 vol.%
2 vol.%
5 vol.%
10 vol.%
20 vol.%
30 vol.%
40 vol.%
50 vol.%
60 vol.%
70 vol.%
80 vol.%
90 vol.%
95 vol.%
100 vol.%
H2 produced (mmol g-1)
Time (h)
(b) ethanol concentration
0 vol.%
1 vol.%
2 vol.%
5 vol.%
10 vol.%
20 vol.%
30 vol.%
40 vol.%
50 vol.%
60 vol.%
70 vol.%
80 vol.%
90 vol.%
95 vol.%
99 vol.%
100 vol.%
H2 produced (mmol g-1)
Time (h)

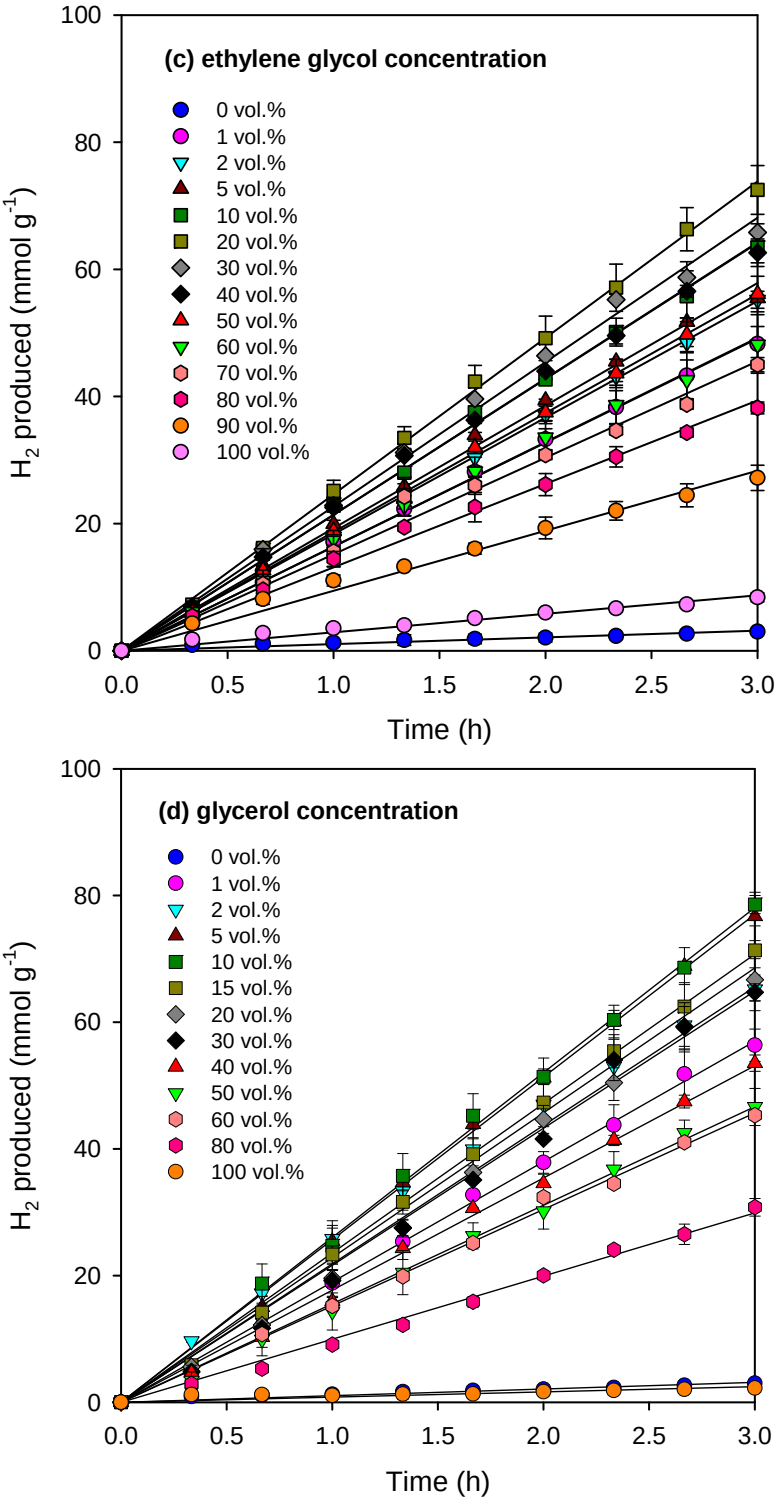
(c) ethylene glycol concentration
0 vol.%
1 vol.%
2 vol.%
5 vol.%
10 vol.%
20 vol.%
30 vol.%
40 vol.%
50 vol.%
60 vol.%
70 vol.%
80 vol.%
90 vol.%
100 vol.%
H2 produced (mmol g-1)
Time (h)
(d) glycerol concentration
0 vol.%
1 vol.%
2 vol.%
5 vol.%
10 vol.%
15 vol.%
20 vol.%
30 vol.%
40 vol.%
50 vol.%
60 vol.%
80 vol.%
100 vol.%
H2 produced (mmol g-1)
Time (h)

Fig. 7

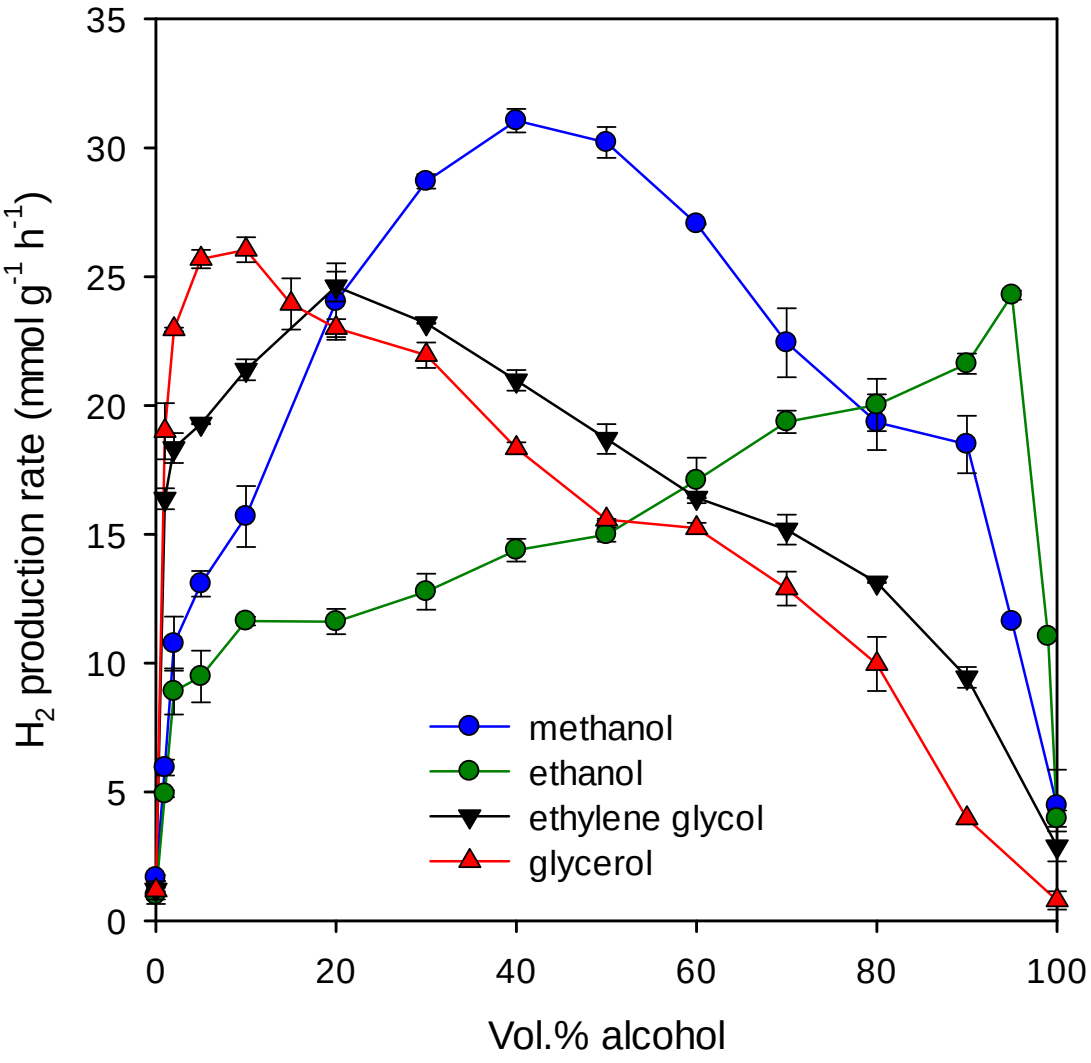
35
30
25
20
15
10
5
0
0
20
40
60
80
100
H2 production rate (mmol g-1 h-1)
Vol.% alcohol
methanol
ethanol
ethylene glycol
glycerol

Fig. 8

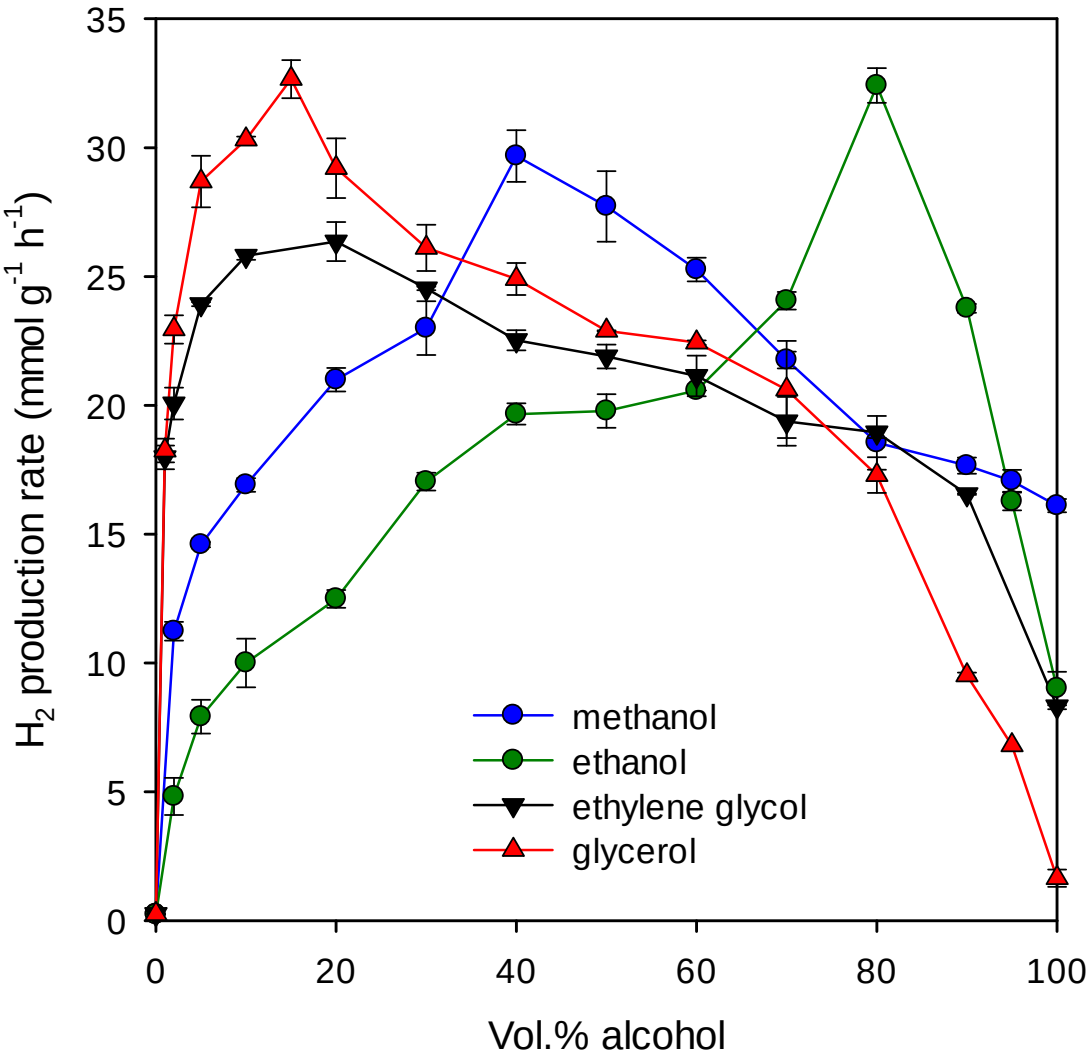
35
30
25
20
15
10
5
0
0
20
40
60
80
100
H2 production rate (mmol g-1 h-1)
Vol.% alcohol
methanol
ethanol
ethylene glycol
glycerol

Fig. 9

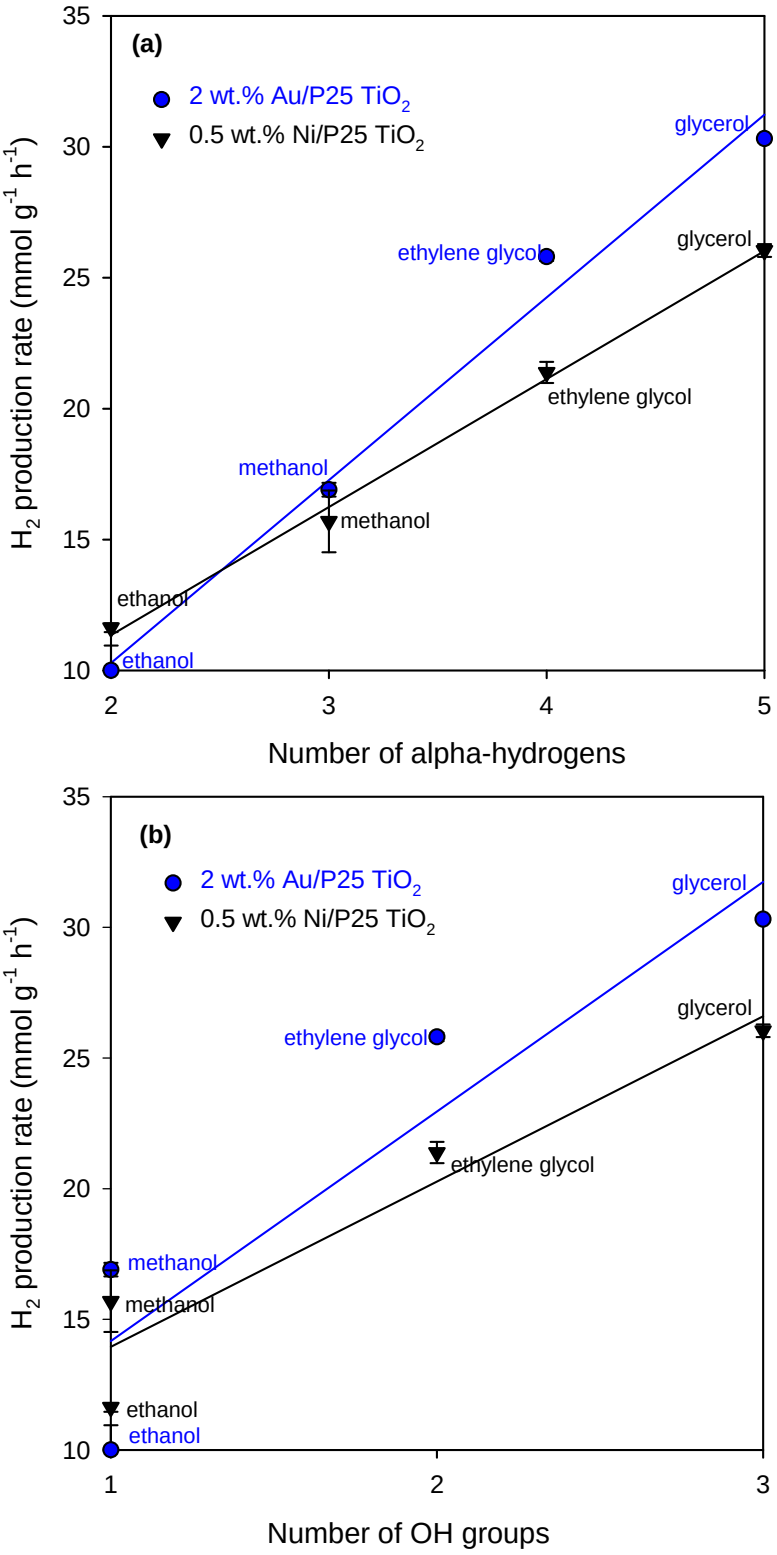
(a)
2 wt.% Au/P25 TiO2
0.5 wt.% Ni/P25 TiO2
glycerol
ethylene glycol
glycerol
ethylene glycol
methanol
methanol
ethanol
ethanol
H2 production rate (mmol g-1 h-1)
Number of alpha-hydrogens
(b)
2 wt.% Au/P25 TiO2
0.5 wt.% Ni/P25 TiO2
glycerol
glycerol
ethylene glycol
ethylene glycol
methanol
methanol
ethanol
ethanol
H2 production rate (mmol g-1 h-1)
Number of OH groups

Fig. 10

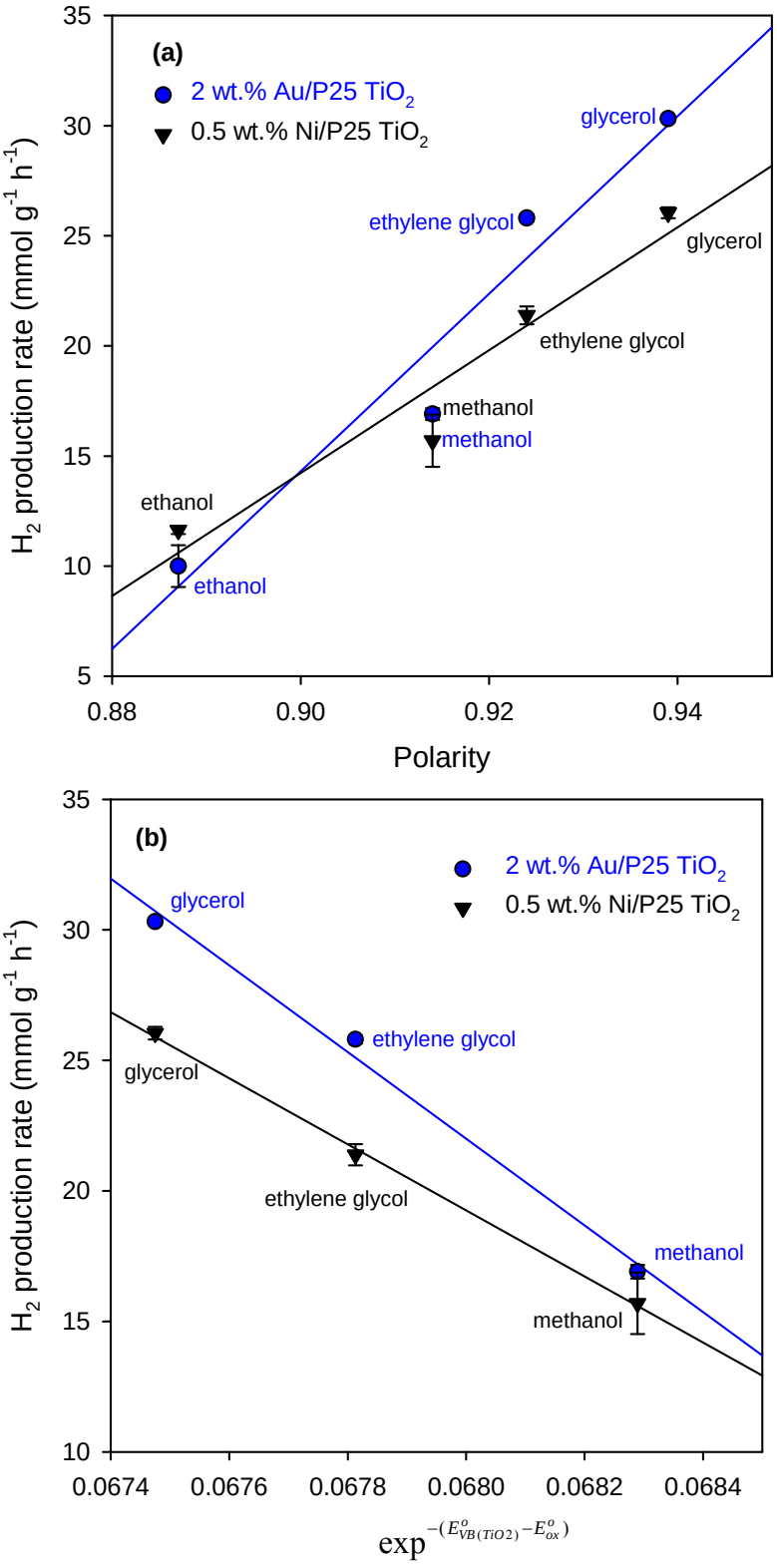
(a)
2 wt.% Au/P25 TiO2
0.5 wt.% Ni/P25 TiO2
glycerol
ethylene glycol
glycerol
ethylene glycol
methanol
methanol
ethanol
ethanol
H2 production rate (mmol g-1 h-1)
Polarity
35
30
25
20
15
10
5
0.88
0.90
0.92
0.94
(b)
2 wt.% Au/P25 TiO2
0.5 wt.% Ni/P25 TiO2
glycerol
ethylene glycol
glycerol
ethylene glycol
methanol
methanol
H2 production rate (mmol g-1 h-1)
exp −(E°VB(TiO2) − E°ox)
35
30
25
20
15
10
0.0674
0.0676
0.0678
0.0680
0.0682
0.0684

Fig. 11

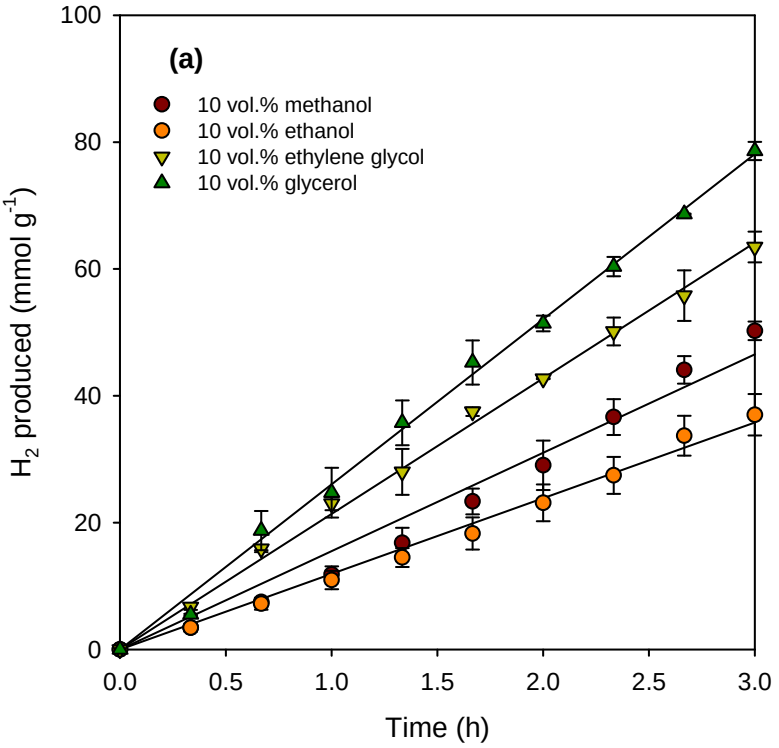
(a)
10 vol.% methanol
10 vol.% ethanol
10 vol.% ethylene glycol
10 vol.% glycerol
H2 produced (mmol g-1)
Time (h)
0
20
40
60
80
100
0.0
0.5
1.0
1.5
2.0
2.5
3.0

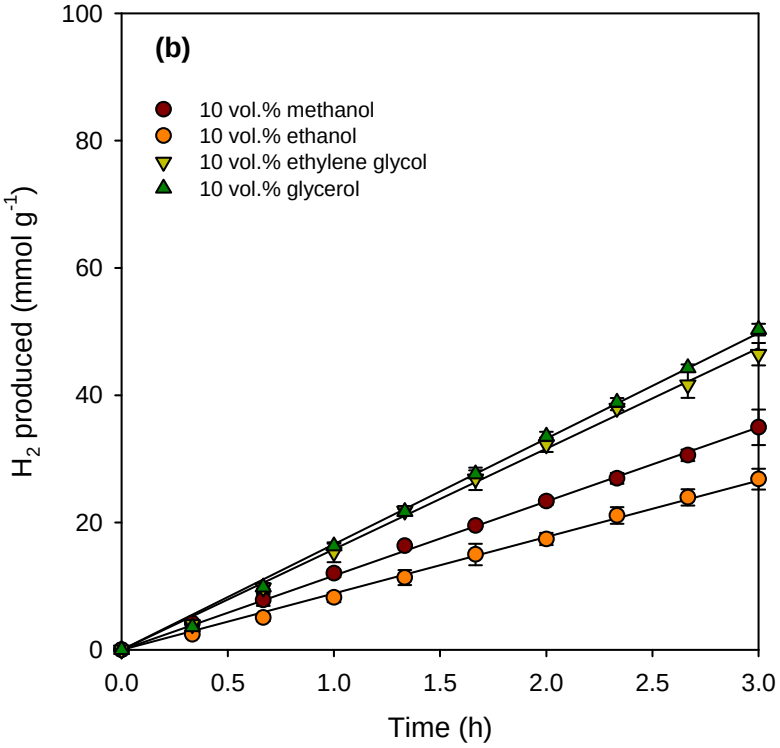
(b)
10 vol.% methanol
10 vol.% ethanol
10 vol.% ethylene glycol
10 vol.% glycerol
H2 produced (mmol g-1)
Time (h)
0
20
40
60
80
100
0.0
0.5
1.0
1.5
2.0
2.5
3.0

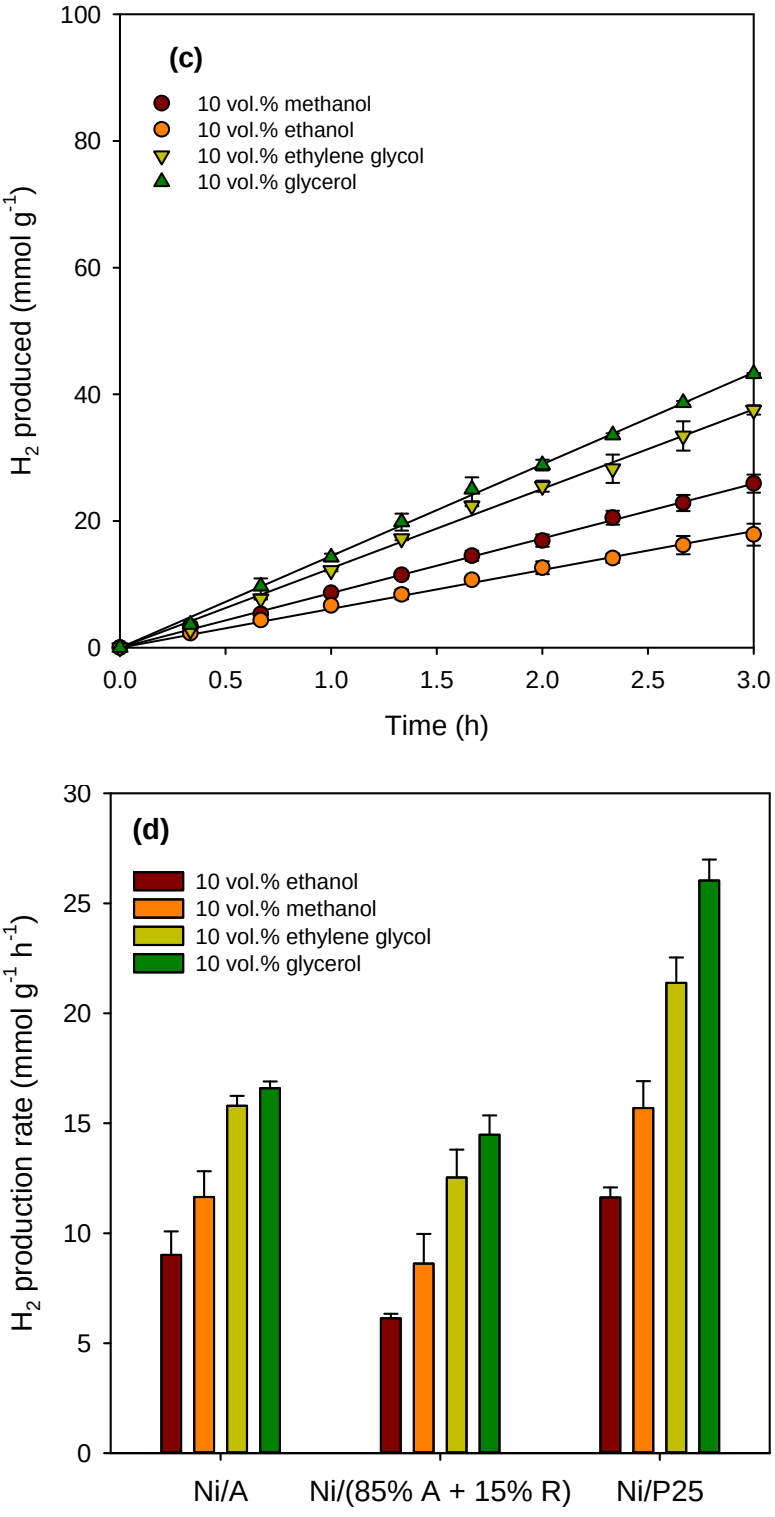
(c)
10 vol.% methanol
10 vol.% ethanol
10 vol.% ethylene glycol
10 vol.% glycerol
H2 produced (mmol g-1)
Time (h)
0
20
40
60
80
100
0.0
0.5
1.0
1.5
2.0
2.5
3.0
(d)
10 vol.% ethanol
10 vol.% methanol
10 vol.% ethylene glycol
10 vol.% glycerol
H2 production rate (mmol g-1 h-1)
0
5
10
15
20
25
30
Ni/A
Ni/(85% A + 15% R)
Ni/P25

Fig. 12

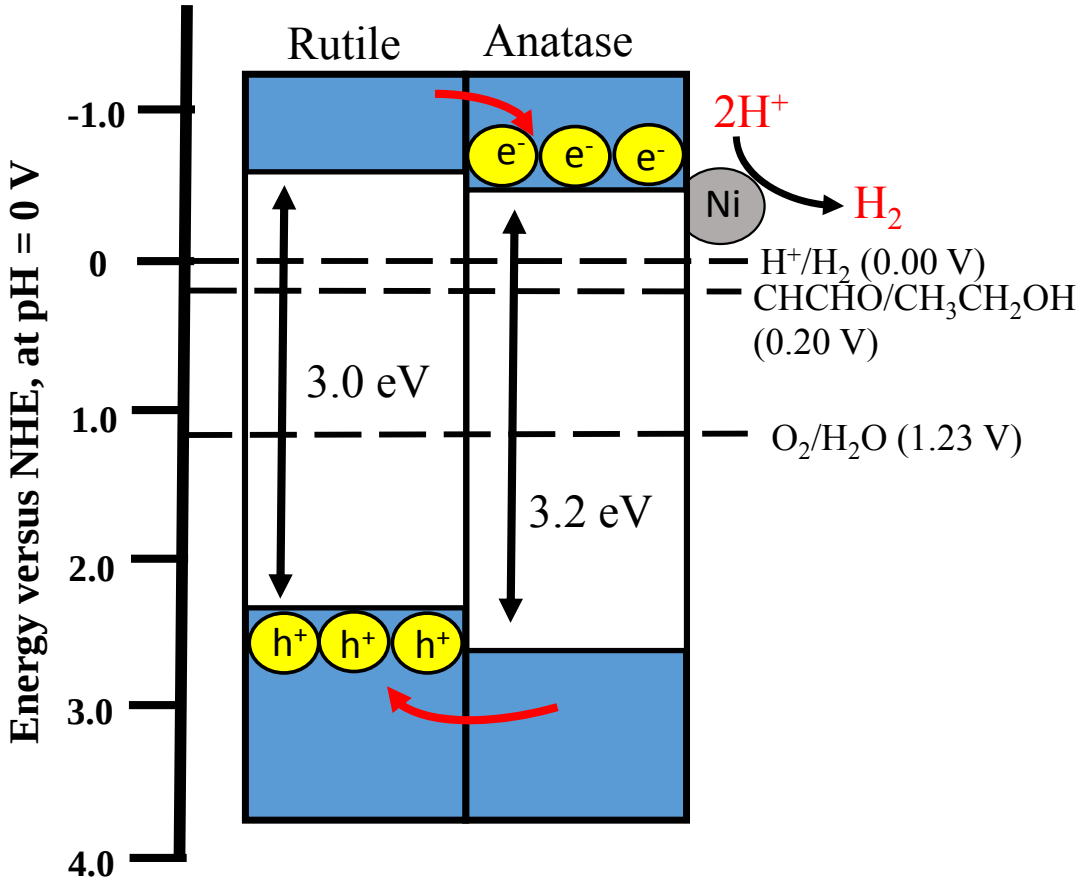
Rutile
Anatase
-1.0
0
1.0
2.0
3.0
4.0
Energy versus NHE, at pH = 0 V
e⁻
e⁻
e⁻
2H⁺
Ni
H₂
H⁺/H₂ (0.00 V)
CHCHO/CH₃CH₂OH
(0.20 V)
3.0 eV
O₂/H₂O (1.23 V)
3.2 eV
h⁺
h⁺
h⁺

Fig. 13

Table 1 — Selection of photocatalytic H_2 production data reported for Ni/TiO_2 and NiO/TiO_2 photocatalysts.

Photocatalysts	Co-catalyst	Optimal co-catalysts loading	Synthesis method	Light source*	Reaction medium	H_2 evolution			
						Rate (µmol g^{-1} h^{-1})	QE (%)	Stability	Ref
Anatase TiO_2	NiO	1.5 wt.%	Single-step sol-gel (SSSG)	UV 300 W (M)	Methanol (10 Vol.%)	813	-	>5 h	[30]
Anatase TiO_2	NiO	1 wt.%	Incipient wetness impregnation (IWI)	UV 300 W (M)	Methanol (10 Vol.%)	587	-	>5 h	[30]
Anatase TiO_2	NiO	1 wt.%	Sol gel	UV 300 W (H)	Methanol (20 vol.%)	617	-	-	[31]
Anatase TiO_2	NiO	1.5 wt.%	Impregnation	UV 450 W (M)	Methanol	80	-	>10 h	[32]
TiO_2	NiO	1.75 wt.%	Sol-gel	Two set of HB175 lamp	Methanol (25 vol.%)	1304	-	8 h	[33]
TiO_2	NiO	0.25 wt.%	Electrospinning method	300 W (X)	Methanol (25 vol.%)	377	1.7	-	[34]
P25 TiO_2	Ni	0.5 wt.%	Complex precipitation	UV SB-100P/F 365 nm	Ethanol (95 vol.%)	20700	-	>24 h	[28]
P25 TiO_2	Ni	0.23 mol.%	Conventional precipitation	Four UV-LEDs 3 W 365 nm	Methanol	3056	12.4	-	[37]
P25 TiO_2	Ni	0.32 mol.%	Photodeposition	350 W (X) 400 nm > λ > 1000 nm	Methanol	2547	8.1	2 h	[38]
Anatase TiO_2	Ni	0.3 wt.%	Simple chemical reduction	UV 150 W (H) 350 nm > λ > 400 nm	Triethanolamine (TEOA)	1000	-	6 h	[39]
Anatase TiO_2	Ni/NiO core/shell	1 wt.%	Impregnation	450 W (X) 350 nm > λ > 450 nm	Pure water	5.5	-	2 h	[40]
P25 TiO_2	Ni/NiO core/shell	1.6 wt.%	Quick ion-impregnation	300 W (X) 420 nm	Eosin Y + Triethanolamine (15 vol.%)	3439	28.6 (at 460 nm)	>5 h	[41]
TiO_2	Ni/NiO	0.5 wt.%	Incipient wetness impregnation	UV irradiation	Methanol	500	8 (at 370 nm)	3h	[13]

M = Mercury lamp, X = Xenon lamp, H = Halogen lamp

Table 2 – Standard oxidation potentials (versus NHE) calculated for the different alcohols used in this study as sacrificial hole scavengers.

Alcohol	**O/C ratio**	**Redox equation for alcohol oxidation** $C_xH_yO_z + (2x-z)H_2O \rightarrow xCO_2 + nH^+ + ne^-$	**Δ_fG^o (kJ mol^{-1})**	**(-)ΔG^o (kJ mol^{-1})**	**Alcohol oxidation potential (V)E_{ox}^o (V)**	**$\exp^{-(E_{VB}-E_{ox})}$**
methanol	1	$CH_4O + H_2O \rightarrow CO_2 + 6H^+ + 6e^-$	-166.6	9.3	0.016	0.0683
ethanol	0.5	$C_2H_6O + 3H_2O \rightarrow 2CO_2 + 12H^+ + 12e^-$	-174.8	97.4	0.084	0.0731
ethylene glycol	1	$C_2H_6O_2 + 2H_2O \rightarrow 2CO_2 + 10H^+ + 10e^-$	-323.2	8.6	0.009	0.0678
glycerol	1	$C_3H_8O_3 + 3H_2O \rightarrow 3CO_2 + 14H^+ + 14e^-$	-477.0	5.1	0.004	0.0675

Δ_fG^o values are taken from "Dean, J. A. (ed.) Lange's Handbook of Chemistry, 15th ed" page 549-594

$-\Delta G^o = x\Delta_fG^o(CO_2) - \Delta_fG^o(C_xH_yO_z) - (2x-z)\,\Delta_fG^o(H_2O)$

E_{ox}^o (V) vs. NHE = $-\Delta G^o/nF$, where n= (4x-2z+y)

$\Delta_fG^o(CO_2)$ = -394.4 kJ mol^{-1}; $\Delta_fG^o(H_2O)$ = -237.1 kJ mol^{-1}; F = 96485 C mol^{-1}

Table 3 — H_2 production rates for 0.5 wt.% Ni/P25 TiO_2 and 2 wt.% Au/P25 TiO_2 in different alcohol-water mixtures under UV irradiation (6.5 mW cm^{-2}).

Alcohol	**H_2 production rate at 10 vol.% alcohol**				**H_2 production rate at 80 vol.% alcohol**			
	0.5 wt.% Ni/P25 TiO_2		2 wt.% Au/P25 TiO_2		0.5 wt.% Ni/P25 TiO_2		2 wt.% Au/P25 TiO_2	
	mmol g^{-1} h^{-1}	mmol m^{-2} h^{-1}*	mmol g^{-1} h^{-1}	mmol m^{-2} h^{-1}*	mmol g^{-1} h^{-1}	mmol m^{-2} h^{-1}*	mmol g^{-1} h^{-1}	mmol m^{-2} h^{-1}*
methanol	15.7	0.350	16.9	0.355	19.3	0.430	18.5	0.390
ethanol	11.6	0.258	10.0	0.210	20.0	0.445	32.4	0.681
ethylene glycol	21.4	0.477	25.8	0.542	13.1	0.292	18.9	0.398
glycerol	26.0	0.579	30.3	0.637	10.0	0.223	17.3	0.363

* BET Surface area for 0.5 wt.% Ni/P25 TiO_2 and 2 wt.% Au/P25 TiO_2 photocatalysts were 44.9 m^2 g^{-1} and 47.6 m^2 g^{-1}, respectively.

Table 4 – Summarized physical properties of the alcohol hole scavengers used in the H_2 production tests.

Alcohol	No. of α-H	No. of OH group	O/C ratio	Solvent Permittivity, ε_s	Polarity*	Refractive Index, n	Polarizability*	Alcohol oxidation potential (V)$^{\neq}$	Optimal alcohol concentration (vol.%)	
									Ni/TiO_2	Au/TiO_2
methanol	3	1	1	32.7	0.914	1.328	0.203	0.016	40	40
ethanol	2	1	0.5	24.6	0.887	1.361	0.221	0.084	95	80
ethylene glycol	4	2	1	37.7	0.924	1.429	0.258	0.009	20	20
glycerol	5	3	1	47.0	0.939	1.475	0.282	0.004	10	15

* Polarity, $Y = (\varepsilon_s - 1)/(\varepsilon_s + 2)$

* Polarizability, $p = (n^2 - 1)/(n^2 + 2)$

≠ Alcohol oxidation potentials were calculated from Gibbs free energies of reaction (see table S1)

Table 5 — H_2 production rates determined for P25 TiO_2 and selected Ni/TiO_2 photocatalysts in different alcohol-water mixtures (alcohol concentration 10 vol.%) under UV irradiation (6.5 mW cm^{-2}).

Sample	**Ni content by XRF (wt.%)**	**Surface area (m^2 g^{-1})**	**H_2 production rate at 10 vol.% alcohol (mmol g^{-1} h^{-1})**			
			methanol	ethanol	ethylene glycol	glycerol
P25 TiO_2	0	49.1	1.4	0.5	1.4	1.9
0.5 wt.% Ni/P25 TiO_2	0.5	44.9	15.	11.6	21.4	26.0
0.5 wt.% Ni/anatase	0.5	38.6	11.6	9.0	15.8	16.6
0.5 wt.% Ni/(85% anatase + 15% rutile)*	0.5	33.2	8.6	6.1	12.5	14.5
0.75 wt.% Ni/P25 TiO_2	0.7	46.0	9.1	7.5	16.9	19.5
1 wt.% Ni/P25 TiO_2	1.1	45.7	6.9	5.3	15.2	17.4

* support consisted of a physical mixture of anatase and rutile nanoparticles isolated from P25 TiO_2 by selective chemical dissolution.

Supplementary information

Performance Comparison of Ni/TiO_2 and Au/TiO_2 Photocatalysts for H_2 Production in Alcohol-Water Mixtures

Wan-Ting Chen[a], Andrew Chan[a], Jordi Llorca[b], Dongxiao Sun-Waterhouse[a], Hicham Idriss[c], Geoffrey I.N. Waterhouse*[a,d]

[a]School of Chemical Sciences, The University of Auckland, Auckland, New Zealand.

[b]Institute of Energy Technologies and Centre for Research in NanoEngineering, Polytechnic University of Catalonia, Digonal 647, 08028 Barcelona, Spain.

[c]SABIC, Corporate Research Institute (CRI), KAUST, Saudi Arabia.

[d]The MacDiarmid Institute for Advanced Materials and Nanotechnology, New Zealand.

*Corresponding author:

Email: g.waterhouse@auckland.ac.nz

Telephone number: 64-9-9237212

Fax number: 64-9-373 7422

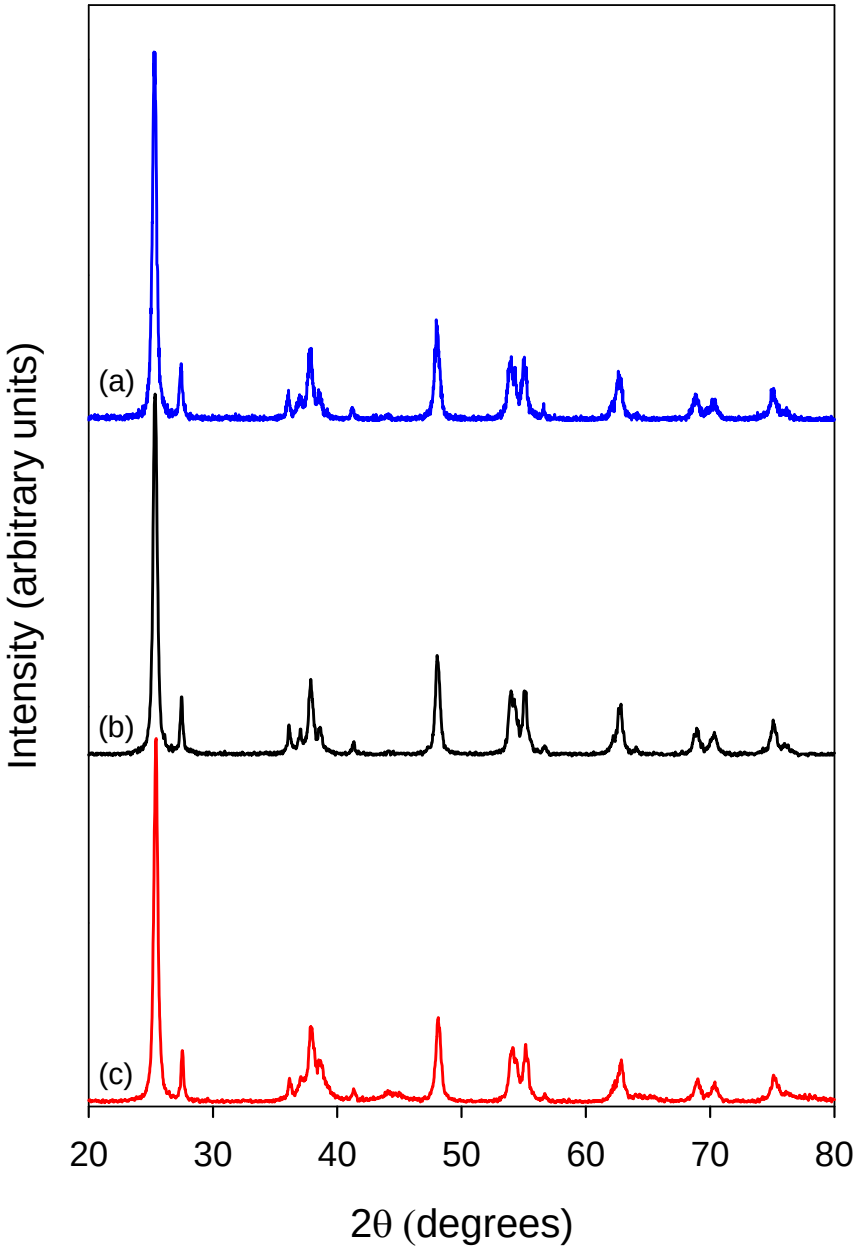

Fig. S1 - Powder XRD patterns for (a) P25 TiO_2; (b) 0.5 wt.% Ni/P25 TiO_2; and (c) 2 wt.% Au/P25 TiO_2 photocatalysts.

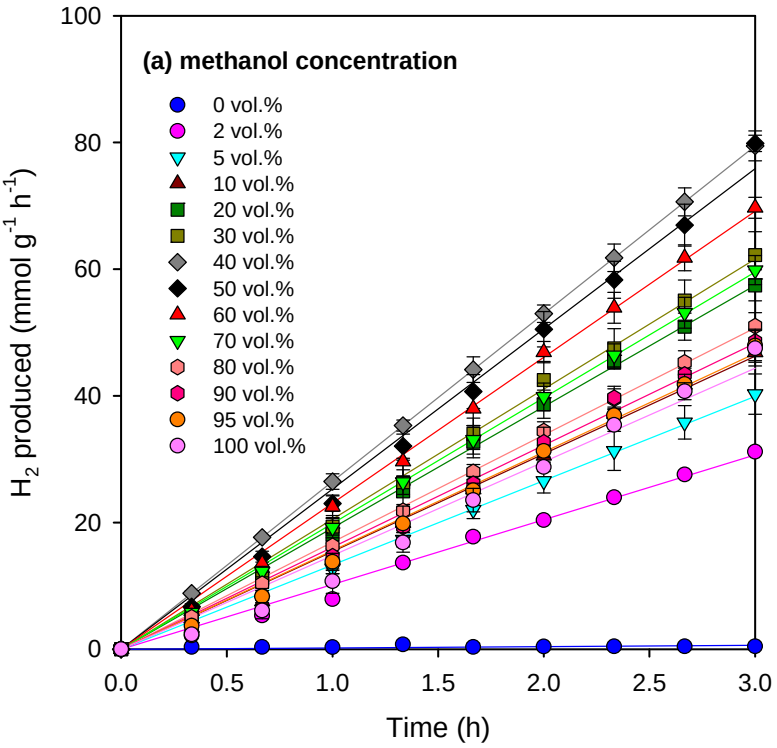
(a) methanol concentration
0 vol.%
2 vol.%
5 vol.%
10 vol.%
20 vol.%
30 vol.%
40 vol.%
50 vol.%
60 vol.%
70 vol.%
80 vol.%
90 vol.%
95 vol.%
100 vol.%
H2 produced (mmol g-1 h-1)
Time (h)
0
20
40
60
80
100
0.0
0.5
1.0
1.5
2.0
2.5
3.0

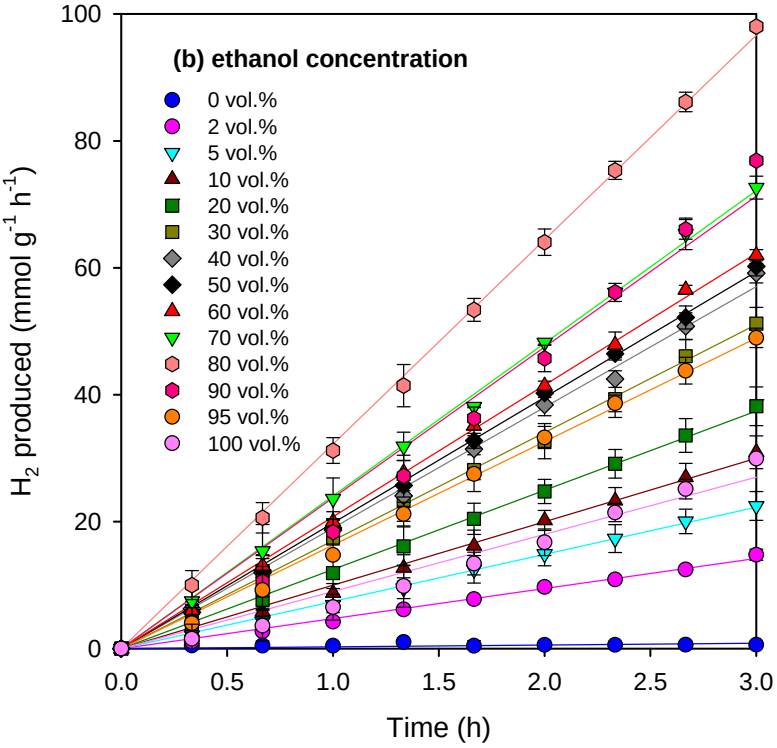
(b) ethanol concentration
0 vol.%
2 vol.%
5 vol.%
10 vol.%
20 vol.%
30 vol.%
40 vol.%
50 vol.%
60 vol.%
70 vol.%
80 vol.%
90 vol.%
95 vol.%
100 vol.%
H2 produced (mmol g-1 h-1)
Time (h)
0
20
40
60
80
100
0.0
0.5
1.0
1.5
2.0
2.5
3.0

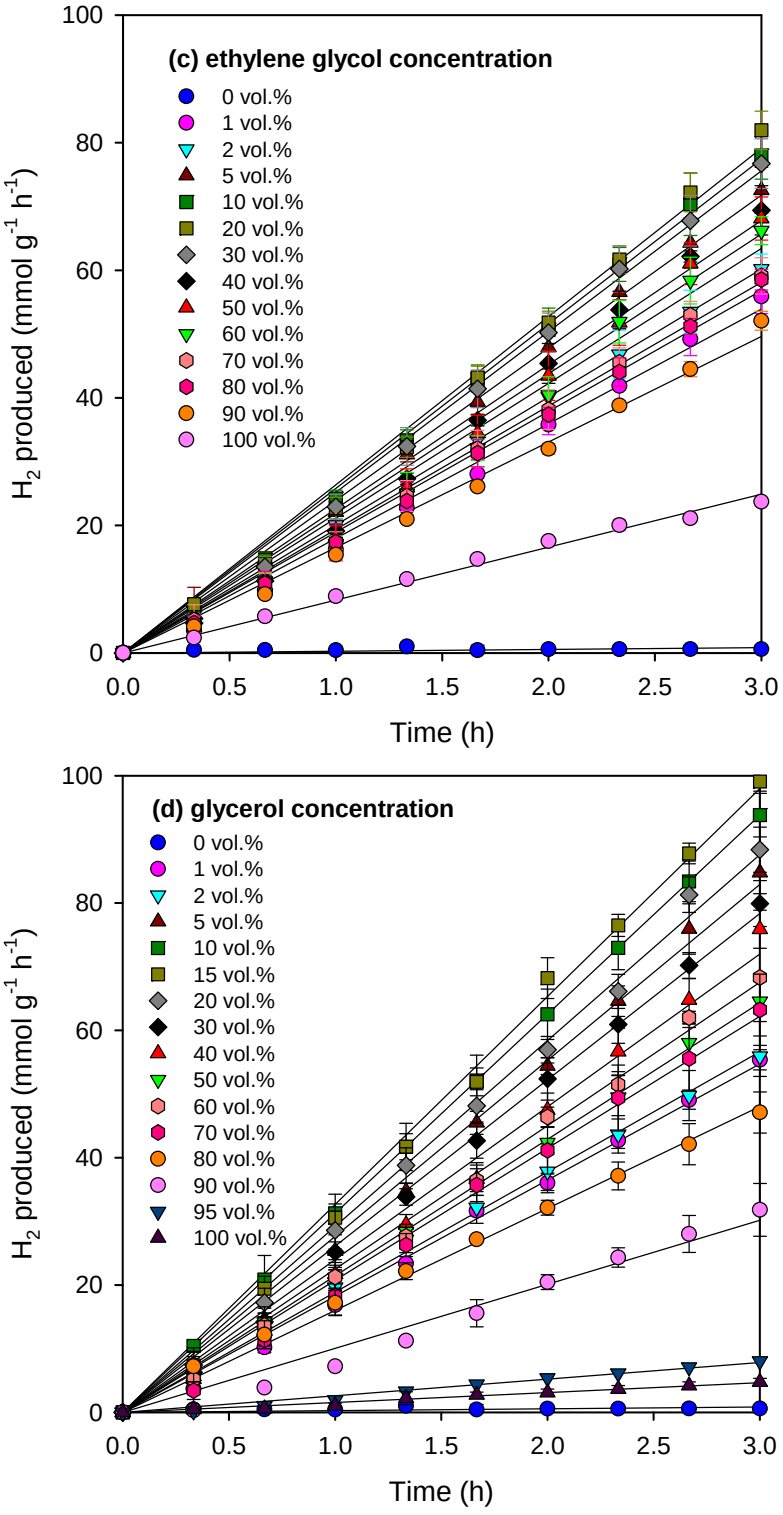

Fig. S2 Plots of H_2 production versus time for 2 wt.% Au/TiO_2 photocatalyst in different alcohol-water mixtures under UV irradiation. (a) methanol; (b) ethanol; (c) ethylene glycol; and (d) glycerol.

Table S1 — H_2 production rates for 0.5 wt.% Ni/P25 TiO_2 and 2 wt.% Au/P25 TiO_2 photocatalysts in different methanol-water mixtures under UV irradiation (6.5 mW cm^{-2}).

Methanol concentration (vol.%)	**Viscosity (cP) at 30 °C***	**Mole ratio H_2O:methanol**	**0.5 wt.% Ni/P25 TiO_2**		**2 wt.% Au/P25 TiO_2**	
			H_2 production rate (mmol g^{-1} h^{-1})	**H_2 production rate (mmol m^{-2} h^{-1})**	**H_2 production rate (mmol g^{-1} h^{-1})**	**H_2 production rate (mmol m^{-2} h^{-1})**
0	0.798	-	1.7	0.037	0.3	0.005
1	-	222.56	5.9	0.132	-	-
2	-	110.15	10.8	0.240	11.2	0.236
5	0.894	42.71	13.1	0.291	14.6	0.307
6	0.992	35.22	14.7	0.328	14.9	0.313
10	1.189	20.23	15.7	0.350	16.9	0.355
20	1.353	8.99	24.0	0.535	21.0	0.441
30	1.465	5.25	28.7	0.639	23.0	0.483
40	1.503	3.37	31.1	0.692	29.7	0.623
50	1.451	2.25	30.2	0.673	27.7	0.582
60	1.330	1.50	27.1	0.602	25.3	0.531
70	1.152	0.96	22.4	0.500	21.8	0.457
80	0.932	0.56	19.4	0.431	18.5	0.390
90	0.831	0.25	18.5	0.412	17.7	0.371
95	0.894	0.12	11.6	0.259	17.1	0.358
100	0.659	0.00	4.5	0.100	16.1	0.338

* Viscosity values were obtained from reference [78].

Table S2 — H_2 production rates for 0.5 wt.% Ni/P25 TiO_2 and 2 wt.% Au/P25 TiO_2 photocatalysts in different ethanol-water mixtures under UV irradiation (6.5 mW cm^{-2}).

Ethanol concentration (vol.%)	**Viscosity (cP) at 30 °C***	**Mole ratio H_2O:methanol**	**0.5 wt.% Ni/P25 TiO_2**		**2 wt.% Au/P25 TiO_2**	
			H_2 production rate (mmol g^{-1} h^{-1})	**H_2 production rate (mmol m^{-2} h^{-1})**	**H_2 production rate (mmol g^{-1} h^{-1})**	**H_2 production rate (mmol m^{-2} h^{-1})**
0	0.798	-	1.0	0.022	0.3	0.005
1	-	321.14	4.9	0.110	-	-
2	0.864	158.95	8.9	0.198	4.8	0.101
5	0.914	61.63	9.5	0.211	7.9	0.166
8	1.086	37.30	10.7	0.238	10.0	0.210
10	1.428	29.19	11.6	0.259	10.3	0.216
20	1.765	12.98	11.6	0.259	12.5	0.262
30	2.036	7.57	12.8	0.284	17.0	0.358
40	2.202	4.87	14.4	0.320	19.7	0.413
50	2.085	3.24	15.0	0.334	19.8	0.416
60	1.905	2.16	17.1	0.381	20.6	0.432
70	1.671	1.39	19.4	0.431	24.1	0.506
80	1.524	0.81	20.0	0.446	32.4	0.681
90	1.425	0.36	21.6	0.482	23.8	0.499
95	0.864	0.17	24.3	0.541	16.3	0.342
99	-	0.03	11.0	0.246	-	-
100	1.280	0.00	4.0	0.088	9.0	0.189

* Viscosity values were obtained from reference [78].

Table S3 — H_2 production rates for 0.5 wt.% Ni/P25 TiO_2 and 2 wt.% Au/P25 TiO_2 photocatalysts in different ethylene glycol-water mixtures under UV irradiation (6.5 mW cm^{-2}).

Ethylene glycol concentration (vol.%)	**Viscosity (cP) at 30 °C***	**Mole ratio H_2O:methanol**	**0.5 wt.% Ni/P25 TiO_2**		**2 wt.% Au/P25 TiO_2**	
			H_2 production rate (mmol g^{-1} h^{-1})	**H_2 production rate (mmol m^{-2} h^{-1})**	**H_2 production rate (mmol g^{-1} h^{-1})**	**H_2 production rate (mmol m^{-2} h^{-1})**
0	0.798	-	1.2	0.027	0.3	0.005
1	-	310.35	16.4	0.365	18.0	0.378
2	0.808	153.61	18.3	0.409	20.1	0.422
5	0.856	59.56	19.3	0.430	23.9	0.503
8	1.019	36.05	20.7	0.462	24.2	0.508
10	1.317	28.21	21.4	0.476	25.8	0.542
20	1.577	12.54	24.6	0.548	26.4	0.554
30	2.131	7.31	23.2	0.517	24.5	0.516
40	2.764	4.70	21.0	0.467	22.5	0.473
50	3.595	3.13	18.7	0.417	21.9	0.460
60	4.866	2.09	16.4	0.366	21.1	0.444
70	6.671	1.34	15.2	0.338	19.4	0.407
80	9.406	0.78	13.1	0.292	18.9	0.398
90	0.808	0.35	9.4	0.210	16.5	0.348
100	13.868	0.00	2.9	0.064	8.3	0.175

* Viscosity values were obtained from reference [78].

Table S4 — H_2 production rates for 0.5 wt.% Ni/P25 TiO_2 and 2 wt.% Au/P25 TiO_2 photocatalysts in different glycerol-water mixtures under UV irradiation (6.5 mW cm^{-2}).

Glycerol concentration (vol.%)	**Viscosity (cP) at 30 °C***	**Mole ratio H_2O:methanol**	**0.5 wt.% Ni/P25 TiO_2**		**2 wt.% Au/P25 TiO_2**	
			H_2 production rate (mmol g^{-1} h^{-1})	**H_2 production rate (mmol m^{-2} h^{-1})**	**H_2 production rate (mmol g^{-1} h^{-1})**	**H_2 production rate (mmol m^{-2} h^{-1})**
0	0.798	-	1.2	0.026	0.3	0.005
1	-	402.00	19.0	0.423	18.2	0.383
2	-	198.97	23.0	0.511	22.9	0.482
5	0.877	77.15	25.7	0.572	28.7	0.603
10	1.030	36.55	26.0	0.580	30.3	0.637
15	1.147	23.01	23.9	0.533	32.7	0.686
20	1.350	16.24	23.0	0.512	29.2	0.614
30	1.907	9.47	22.0	0.489	26.1	0.549
40	2.720	6.09	18.3	0.408	24.9	0.523
50	4.210	4.06	15.6	0.347	22.9	0.481
60	9.850	2.71	15.2	0.339	22.4	0.471
70	21.200	1.74	12.9	0.287	20.6	0.433
80	33.900	1.02	10.0	0.222	17.3	0.363
90	147.000	0.45	4.0	0.089	9.5	0.200
95	-	0.21	-	-	6.8	0.143
100	612.00	0.00	0.8	0.018	1.6	0.035

* Viscosity values were obtained from reference [79].

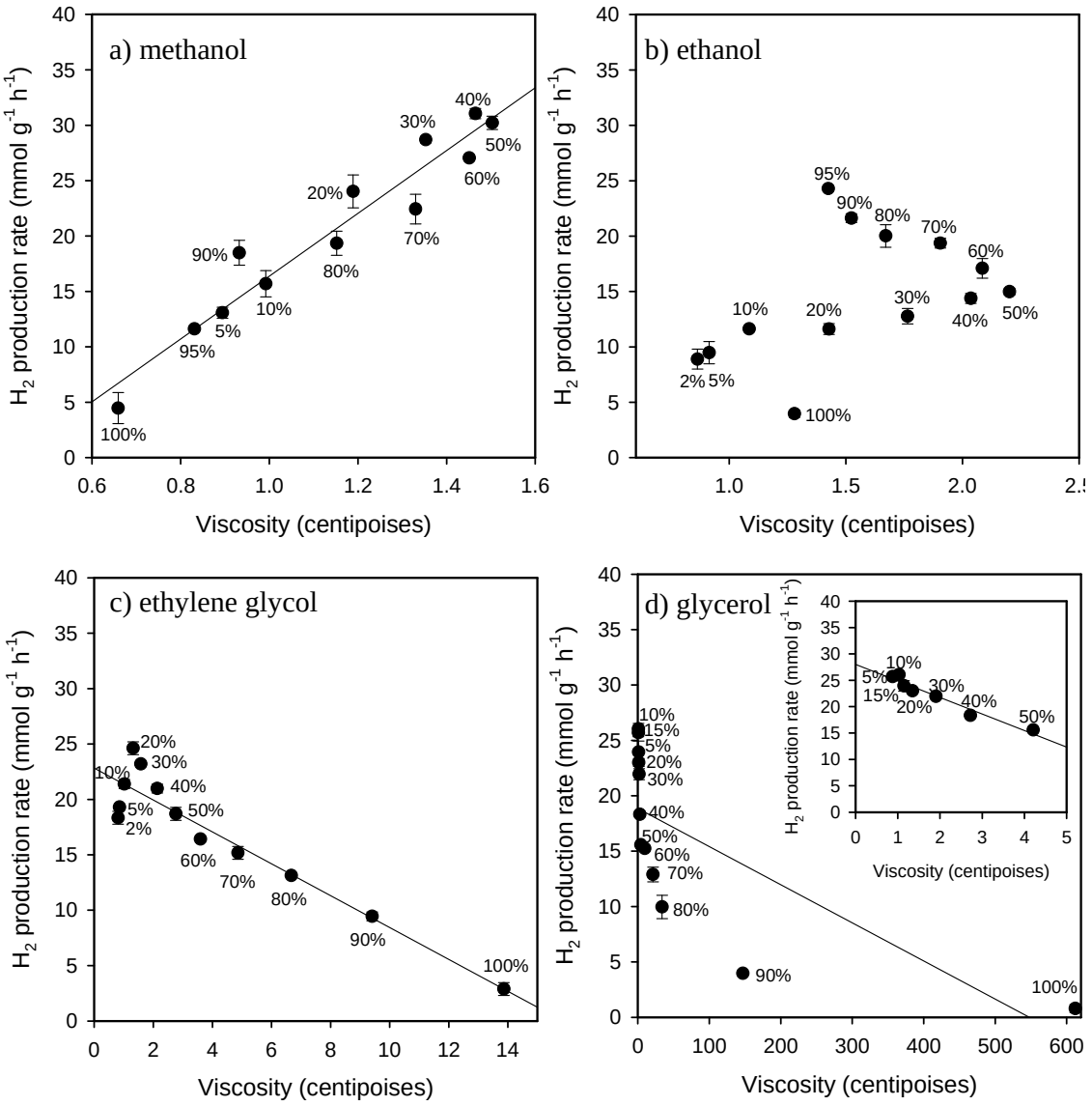

Fig. S3 Plots of H_2 production rate versus the viscosity of alcohol-water mixtures for 0.5 wt.% Ni/TiO_2. (a) methanol; (b) ethanol; (c) ethylene glycol; and (d) glycerol.

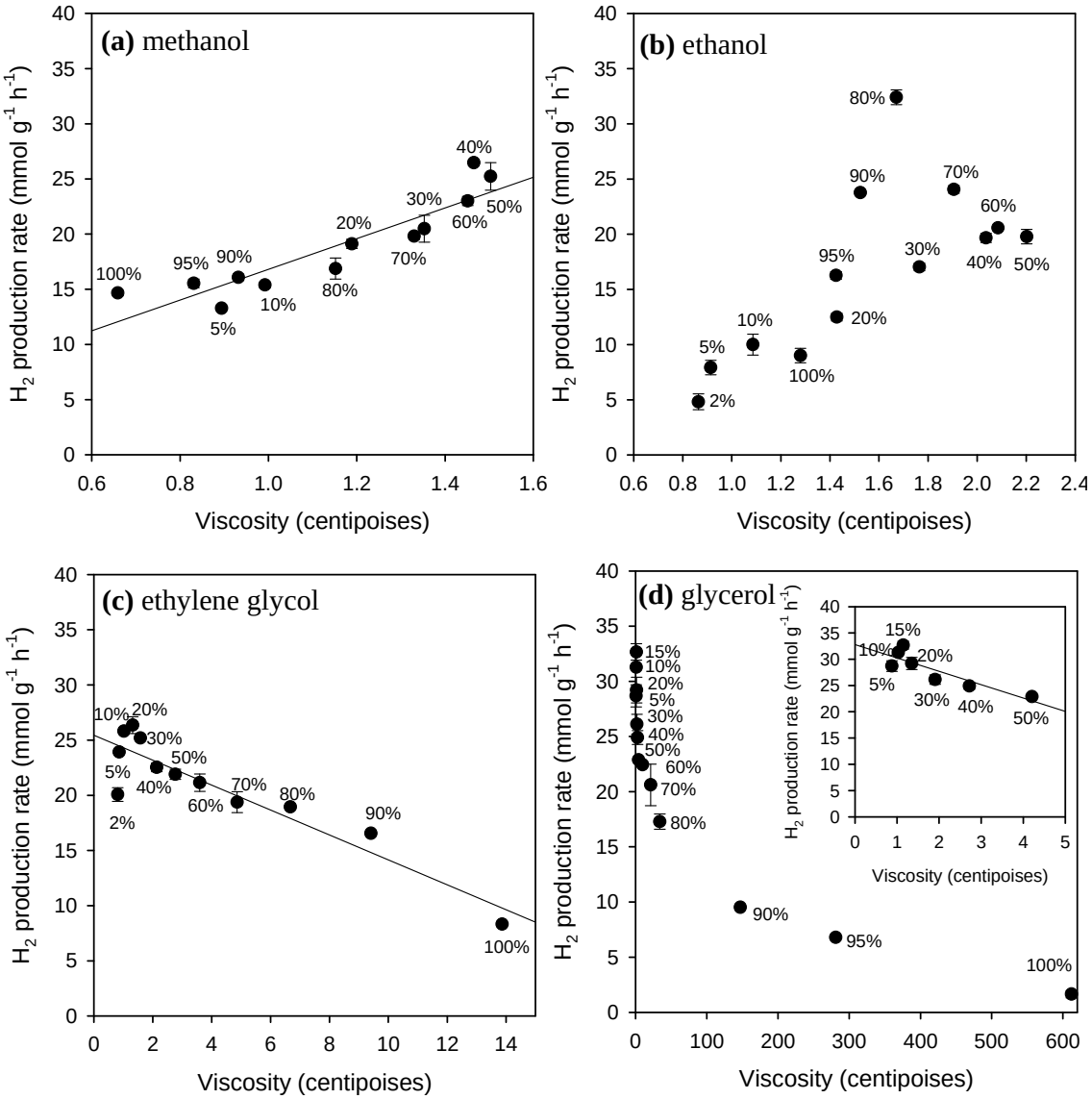

Fig. S4 Plots of H_2 production rate versus the viscosity of alcohol-water mixtures for 2 wt.% Au/TiO_2. (a) methanol; (b) ethanol; (c) ethylene glycol; and (d) glycerol.

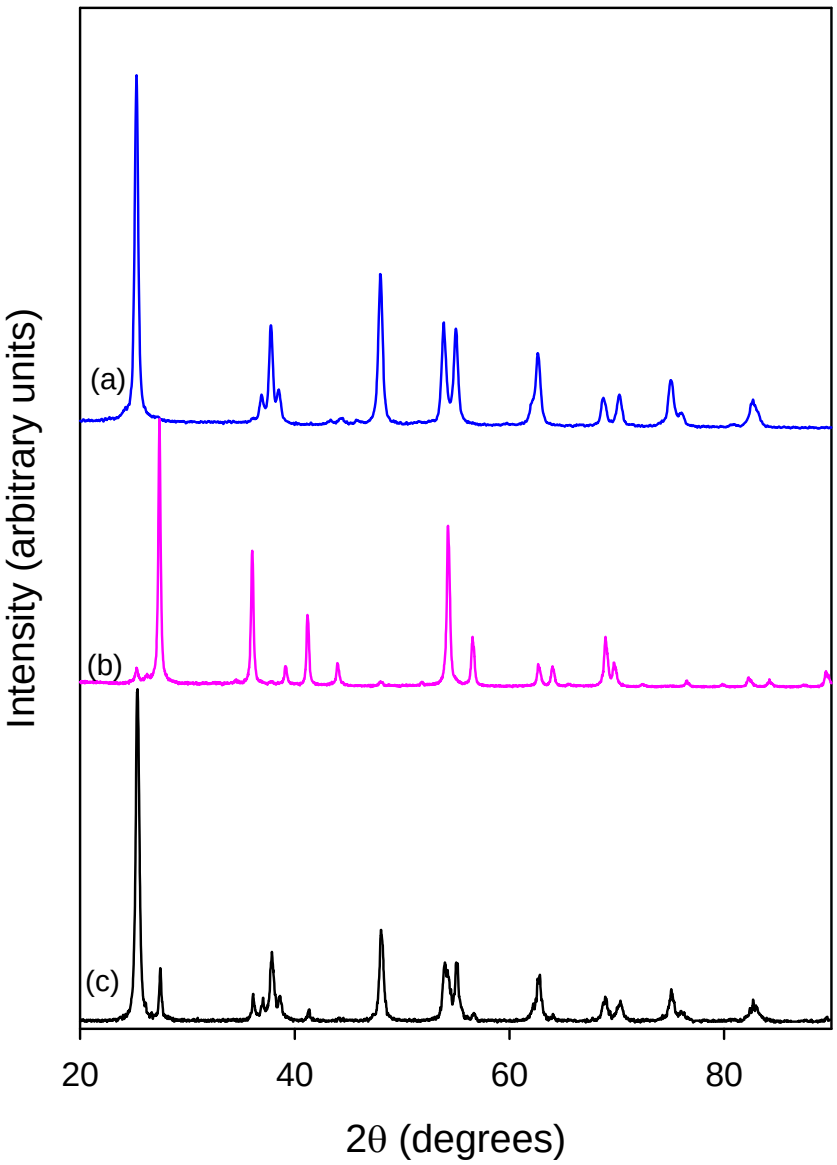

Fig. S5 – XRD for (a) anatase from P25 TiO_2; (b) rutile from P25 TiO_2; and (c) P25 TiO_2 photocatalysts.